

Article

# Multiphasic protein condensation governed by shape and valency

Q1 Vikas Pandey,<sup>1,2,3</sup> Tomohisa Hosokawa,<sup>4</sup> Yasunori Hayashi,<sup>4</sup> and Hidetoshi Urakubo<sup>1,2,3,5,\*</sup>

<sup>1</sup>Department of Biomedical Data Science, Fujita Health University School of Medicine, 1-98 Dengakugakubo, Kutsukake-cho, Toyoake 470-1192, Japan

<sup>2</sup>International Center for Brain Science (ICBS), Fujita Health University, 1-98 Dengakugakubo, Kutsukake-cho, Toyoake 470-1192, Japan

<sup>3</sup>National Institute of Physiological Sciences, National Institutes of Natural Sciences, 5-1 Myodaiji-Higashiyama, Okazaki 444-8787, Japan

<sup>4</sup>Department of Pharmacology, Kyoto University Graduate School of Medicine, Kyoto 606-8501, Japan

<sup>5</sup>Lead contact

\*Correspondence: [hurakubo@gmail.com](mailto:hurakubo@gmail.com)

<https://doi.org/10.1016/j.celrep.2025.115504>

## SUMMARY

Liquid-liquid phase separation (LLPS) of biological macromolecules leads to the formation of various membraneless organelles. The multilayered and multiphasic form of LLPS can mediate complex cellular functions; however, the determinants of its topological features are not fully understood. Herein, we focus on synaptic proteins consisting of Ca<sup>2+</sup>/calmodulin-dependent protein kinase II (CaMKII) and its interacting partners and present a computational model that reproduces forms of LLPS, including a form of two-phase condensates, phase-in-phase (PIP) organization. The model analyses reveal that the PIP formation requires competitive binding between the proteins. The PIP forms only when CaMKII has high valency and a short linker length. Such CaMKII exhibits low surface tension, a modular structure, and slow diffusion, enabling it to stay in small biochemical domains for a long time, which is necessary for synaptic plasticity. Thus, the computational

Q2 modeling reveals new structure-function relationships for CaMKII as a synaptic memory unit.

## Q3 Q4 Q7 INTRODUCTION

Liquid-liquid phase separation (LLPS) is an emerging concept in biology in which macromolecules spontaneously form condensates, often occurring in nucleic acids and proteins with multivalent domain interactions or intrinsically disordered regions (IDRs).<sup>1-3</sup> LLPS leads to the formation of organelles that lack membranes, such as transcription and translational machineries, ribonucleic acid (RNA) granules, stress bodies, nucleoli, and chromosomes, and postsynaptic density (PSD).<sup>4-6</sup> By concentrating and organizing molecules in a small domain, LLPS facilitates the reactions mediated by these organelles. The functions of the condensates can be further elaborated using more complex forms of LLPS. Two or more phases with different components can coexist in a single condensate in various topological configurations such as phase-in-phase (PIP), partially engulfed, or phase-on-phase structures (Figure 1A).<sup>4,7,8</sup> The topological structure of a multicomponent condensate is influenced by interfacial tensions,<sup>9-11</sup> competitive binding,<sup>11,12</sup> and charge patterning in IDRs,<sup>13</sup> and such characteristics help cells to organize cellular components in functionally related subdomains.<sup>14,15</sup> For instance, a two-phase condensate with outer- and inner-phase layers can facilitate sequential reactions; a molecule in the diluted phase must pass through the outer phase before reaching the inner phase, thereby forcing the reaction mediated by the outer layer to occur before that in the inner core.<sup>16</sup> Furthermore, because of Ostwald ripening, wherein small condensates

spontaneously merge into a larger condensate, small condensates in a microdomain cannot persist, at least in principle.<sup>17,18</sup> This phenomenon may be circumvented by wrapping an inner phase with an outer phase exhibiting low surface tension.<sup>7,18,19</sup> However, the factors that determine the topology have not been fully theoretically accounted for. Given that attempts to target LLPS as a therapeutic approach have already begun,<sup>20-22</sup> a thorough understanding of the mechanism governing a multicomponent and multiphasic condensate is critical.

The factors that determine the efficacy with which a molecule undergoes LLPS have been examined using simulations, including Monte Carlo (MC) and molecular dynamics (MD) simulations.<sup>23,24</sup> This approach enables efficient phase-plane analyses to determine the topological changes induced by continuous variables, such as concentration.<sup>25</sup> Consistently, studies targeting linear RNA-binding proteins have demonstrated that multiphase condensates are dependent upon molecular concentration because of the competitive binding between different molecular species.<sup>11,12</sup> The effect of linkers connecting interaction domains has also been examined for monomeric linear multivalent molecules<sup>26-30</sup>; however, domains exhibiting LLPS are often not linearly connected; rather, they are branched or spread radially, which increases the overall complexity.<sup>7,31,32</sup>

Here, we identified the mechanisms of multiphase condensate formation using four synaptic proteins: CaMKII, *N*-methyl-D-aspartate (NMDA) receptor subunit GluN2B, PSD protein 95 (PSD-95), and  $\alpha$ -amino-3-hydroxy-5-methyl-4-isoxazolepropionic

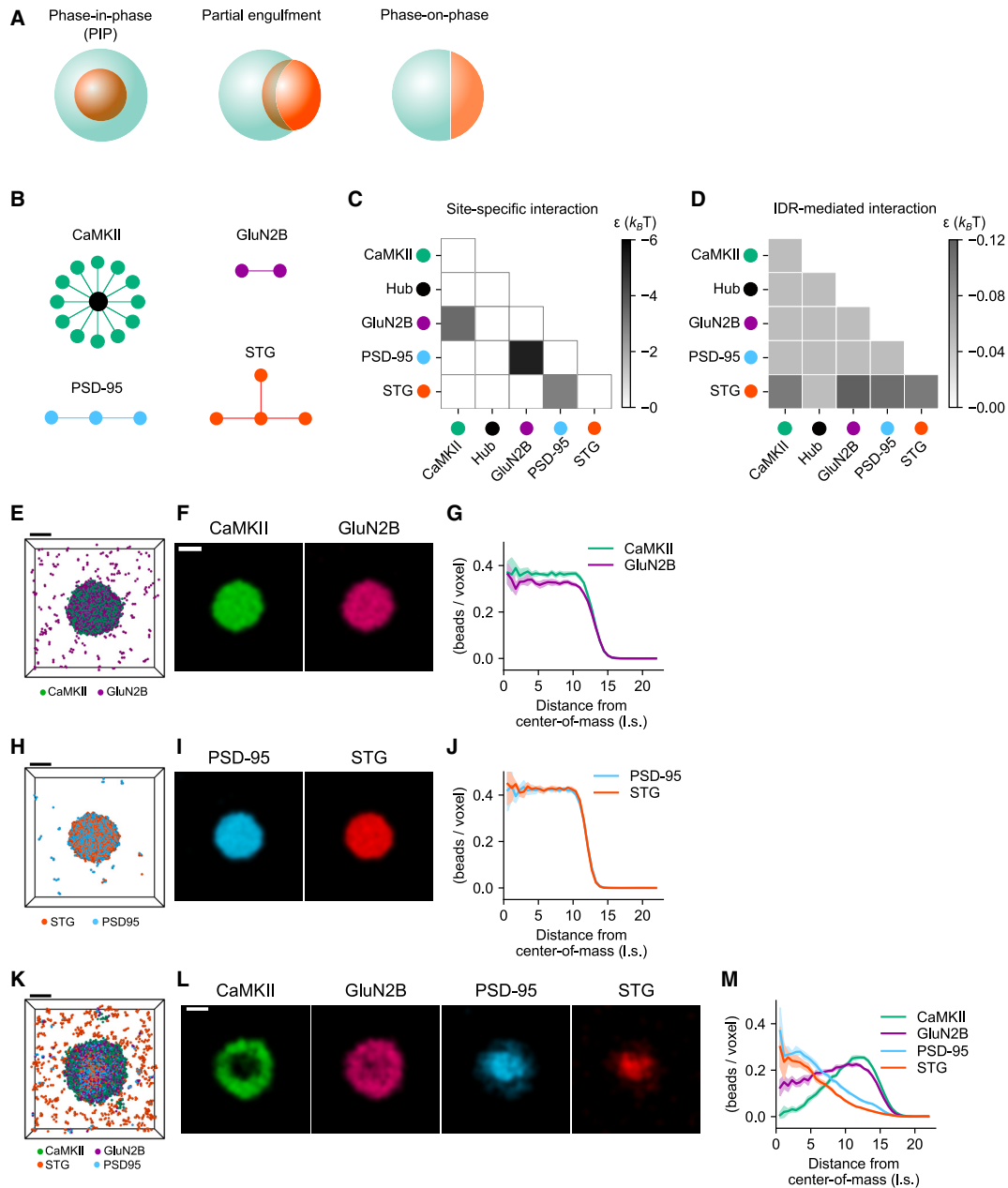


**Figure 1. Various LLPS are reproduced in the Monte Carlo (MC) simulation of postsynaptic proteins**

(A) Topological characteristics of the two-phase condensate. Depending on the surface and interfacial tensions, the two-phase condensate exhibited phase-in-phase (PIP) (left), partially engulfed (center), or even phase-on-phase structures.<sup>4,7</sup>

(B) To examine the multiphase condensates at postsynaptic spines, we modeled four synaptic proteins as a combination of beads and linkers. Filled circles denote beads, each of which occupied a lattice site, and lines denote linkers that connect two beads.

(C) Interaction matrix for site-specific interactions.  $\epsilon$  denotes binding energy (see STAR Methods).

(D) Interaction matrix for the intrinsically disordered region (IDR)-mediated interactions.

(E–G) Simulated condensate of the binary mixture of CaMKII and GluN2B. (E) Protein distribution in the three-dimensional reaction space. The front half was removed, and only the rear half is shown for visibility. (F) Normalized concentration levels at the section that divides the center of the condensate. (G) Radial distribution profiles (RDPs) of protein concentrations from the center of the condensate.

(H–J) Simulated condensate of the binary mixture of CaMKII and GluN2B.

(K–M) Simulated condensate of the mixture of all four proteins. Scale bar, 10 l.s.

Means and standard deviations (SDs) in (G), (J), and (M) were obtained based on data at five sampling times (STAR Methods). See Figure S1.

acid (AMPA) receptor-auxiliary subunit stargazin (STG). CaMKII has recently been shown to play a structural role at the synapse not just acting as a kinase mediating cellular signaling.<sup>33,34</sup> This role is mediated by  $\text{Ca}^{2+}$ /calmodulin-induced LLPS of the kinase domain of CaMKII with its binding partners, which include the carboxyl tail of GluN2B,<sup>5,16</sup> through its rotationally symmetric dodeca- or tetradecameric structure.<sup>35</sup> The ternary mixture of STG-PSD-95-GluN2B forms a homogeneous condensate.<sup>16,36</sup> When CaMKII is present in the absence of  $\text{Ca}^{2+}$ /calmodulin, CaMKII remains in the diluted phase, whereas STG-PSD-95-GluN2B still forms a homogeneous condensate. However, when  $\text{Ca}^{2+}$ /calmodulin is added to stimulate CaMKII, CaMKII organizes on the condensate as in PIP form; the CaMKII-GluN2B predominantly resides in the outer layer, whereas STG-PSD-95 occupies the inner core of this condensate.<sup>7,11,16,37</sup> This structure persists even after the calcium is chelated by ethylene glycol tetraacetic acid, which is consistent with the maintenance of long-term potentiation.<sup>35</sup> This spatial segregation facilitates the segregation of AMPA and NMDA receptors, thereby facilitating efficient neurotransmission.<sup>16</sup> Because the same set of proteins can assume different topological configurations of condensates depending on the conditions, we deemed that these proteins offer a versatile model for understanding the mechanism of the formation of multiphasic LLPS.

Therefore, we used the MC method on the Lattice-Based Structure and Stability Investigation (LaSSI) simulation engine to model protein shapes and interactions and simulate their collective behaviors.<sup>7,9,10,38–41</sup> The model was built with a biologically plausible set of parameters that reproduced various experimentally observed LLPS,<sup>16,36,42–44</sup> and the simulated concentration dependence revealed that competitive binding to PSD-95 is required for the PIP formation. Through alterations in the CaMKII shape, we found that high valencies through the rotationally symmetric dodecameric structure and short linker length were both required for the PIP. The short linker length created a low surface tension, which is required to form the outer phase of the PIP structure, while the high valency is required for the condensate formation itself. The simulation results also implied that the modular structure formation in the CaMKII-GluN2B condensate caused the slow diffusion of CaMKII. These results revealed new structure-function relationships for CaMKII as a synaptic memory unit. This is the first systematic and mechanistic study investigating the divergent structure of protein-regulated multiphase condensates.

## RESULTS

### A minimal model of postsynaptic proteins reproduces the various forms of LLPS

To elucidate the mechanisms of condensate formation involving postsynaptic proteins, we used the LaSSI simulation engine, which handles MC simulations in a three-dimensional (3D) lattice space where each lattice site is occupied by one bead, to simulate the collective behaviors of proteins.<sup>38</sup> Updates of bead locations are based on the Metropolis-Hastings algorithm, which considers binding energies and spatial constraints, and its fast computation is advantageous for studying cellular-level LLPS.<sup>7,9,10,38–41</sup>

We first modeled the shapes of CaMKII, GluN2B, PSD-95, and STG (Figure 1B). CaMKII was modeled as a combination of 12 binding beads representing the kinase domain and a hub bead representing the association domain (Figure 1B, top left). Each pair of hub and binding beads was connected by a linker whose maximal length was 3 lattice sites (l.s.), where l.s. denotes the unit length (see STAR Methods). Those connections represented the hub-and-spoke architecture of CaMKII (Figure 1B, top left). GluN2B was modeled as a pair of beads, mimicking the endogenous tetrameric receptor complex with GluN1 (Figure 1B, top right).<sup>16</sup> PSD-95 was modeled as a series of three beads, each representing a PDZ domain (Figure 1B, bottom left). STG was modeled as T-shaped tetrameric beads representing the tetrameric, concentrated, and small-sized structure of STG.<sup>16</sup> The maximal linker lengths between the GluN2B, PSD-95, and STG beads were all set as 2 l.s. (see STAR Methods). Throughout shape modeling, we modeled only the schematic characteristics of the proteins (e.g., CaMKII consisting of a center hub tethering 12 binding subunits with equal accessibility) but did not incorporate other details, such as the double hexameric structure of CaMKII.<sup>45</sup> We aimed to develop a minimal model of protein shapes that reproduce the experimentally observed forms of LLPS.

Herein, we modeled the site-specific interactions between the CaMKII binding beads and GluN2B, GluN2B and PSD-95, and PSD-95 and STG (Figure 1C). The binding energies of these site-specific interactions<sup>42,46</sup> were determined based on previous experimental studies (see STAR Methods). The site-specific interactions were modeled as the anisotropic interactions of LaSSI as one-to-one (mutually exclusive) and anisotropic.

We further modeled IDR-mediated interactions. As shown in Figure 1D, all constituent beads were set to be associated with two orders of magnitude weaker than the site-specific interactions (see STAR Methods).<sup>9,10</sup> The carboxyl tails of GluN2B and STG, both of which were incorporated in *in vitro* experiments, are indeed IDRs, and the carboxyl tail of STG and PSD-95 is known to interact through their IDRs, which is attributed to the presence of arginine-rich segments.<sup>36</sup> These interactions were modeled as the isotropic interactions of LaSSI and were therefore one-to-many and isotropic. Other details, including the simulation time schedule, are described in the STAR Methods.

To validate the constructed model, we first simulated binary mixtures of CaMKII-GluN2B, PSD-95-STG, and GluN2B-PSD-95 (Figures 1E–1J and S1A–S1C). Consistent with the preceding experimental and computational evidence,<sup>16,36,47</sup> they all showed homogeneous condensation (Figures 1E–1J and S1A–S1C) and remained spherical as shown in their 3D profiles (Figures 1E, 1H, and S1A). Their sectional images revealed the homogeneity of the condensate (Figures 1F, 1I, and S1B), and the radial distribution profiles (RDPs) from the center of mass showed a quantitative uniform distribution (Figures 1G, 1J, and S1C). The ternary mixture of CaMKII-GluN2B-PSD-95 also underwent homogeneous condensation, which is again consistent with results from a previous study (Figures S1D–S1F).<sup>48</sup>

The quaternary mixture of CaMKII, GluN2B, PSD-95, and STG underwent PIP condensation (Figures 1K–1M). CaMKII and GluN2B, located at the periphery of the condensate, formed

the shell phase, while PSD-95 and STG, concentrated at its center, formed the core phase (Figures 1K–1M). The core formation presumably came from the tight coupling of PSD-95 and STG and GluN2B and its binding partner; CaMKII, was relegated to the periphery presumably because the CaMKII-GluN2B phase had a low surface tension.<sup>7,9–11,13,37</sup> PIP condensation similarly appeared even if CaMKII exhibited a more realistic double hexamer structure (Figures S1J–S1N). In contrast, when inactive CaMKII, GluN2B, PSD-95, and STG were mixed, the inactive CaMKII was dissipated in the diluted phase, and the latter three phases underwent homogeneous condensation (Figures S1G–S1I). Here, inactive CaMKII denotes the CaMKII devoid of the interactions, mimicking an inactive, closed conformation of the enzyme. Upon activation of CaMKII, the homogeneous condensate was transformed into a PIP condensate structure (Video S1). This transition occurred autonomously, ensuring that PIP formation was independent of the initial spatial distribution of the proteins. Overall, our simulations successfully reproduced the various forms of phase-separated structures and their mesoscopic characteristics, validating the reliability of this model.

#### Experimentally observed concentration dependence aligns with the computational model

We then tested the concentration dependency of the PIP organization in the model (Figures 2A–2C, top). When we decreased the concentration of STG by 3-fold or less, the condensate became homogeneous. Similarly, when we increased the concentration of GluN2B and STG simultaneously by 1.5-fold or more, the condensate also became homogeneous. Their topological shapes were clearly characterized in their rendered 3D shapes (Figures 2A–2C, bottom left). To validate our simulation, we performed biochemical experiments using fluorescently labeled recombinant proteins (see STAR Methods; Figures 2D–2F). The control set of concentrations (i.e., 20  $\mu\text{M}$  CaMKII, 5  $\mu\text{M}$  GluN2B, 20  $\mu\text{M}$  PSD-95, and 15  $\mu\text{M}$  STG) exhibited PIP organization (Figure 2D). Conversely, a 3-fold decrease in STG concentration to 5  $\mu\text{M}$  produced homogeneous condensates instead of PIP organization (Figure 2E). Furthermore, a simultaneous 2-fold increase of GluN2B and STG concentration (10 and 30  $\mu\text{M}$ , respectively) produced a homogeneous condensate (Figure 2F). A small heterogeneity in the homogeneous condensate (Figures 2B and 2C) was also consistent with the simulation (Figure 2F). Overall, both simulation and biochemical experiments confirmed that PIP organization did not always appear but depended on the specific protein concentrations.

Further simulation revealed the requirement of minimal GluN2B for the CaMKII-GluN2B condensation. At a GluN2B concentration below a threshold level, the CaMKII-GluN2B condensate did not appear and only the STG-PSD-95 condensate appeared (e.g.,  $0.31 \times 10^{-3}$  beads/voxel in Figure 2G, bottom; blue-shaded region in Figure 2H). Similarly, if the concentration of GluN2B exceeded a certain level (gray-shaded region in Figure 2H), this led to well-mixed homogeneous condensate comprising the four proteins (e.g.,  $10.0 \times 10^{-3}$  beads/voxel in Figure 2G). If the STG concentration was  $>1.5 \times 10^{-3}$  beads/voxel, in some cases the two-phase condensates formed a partial engulfment, but not a PIP (white region in Figure 2H). Together, the two-phase condensates of the quaternary mixture

appeared only in the appropriate concentration range of GluN2B and STG (red and white regions in Figure 2H). As summarized in the phase diagram (Figures 2H and S2A), each form clearly occupied its own concentration range, suggesting the existence of underlying mechanisms.

#### PSD-95 sharing is required for PIP

We next examined the role of the site-specific interaction between CaMKII and GluN2B. This interaction was important for the CaMKII-GluN2B phase of the PIP organization. The average number of GluN2B proteins bound to one CaMKII almost completely reflected the concentration of GluN2B (Figure 3A) and corresponded to the volume of the CaMKII condensate ( $R^2 = 0.97$ , Figure 3B). Here, the CaMKII condensate was defined as the region of the largest volume among the group of regions where the CaMKII concentration exceeded the half-maximal level (STAR Methods).

Similarly, we examined the site-specific interaction between STG and PSD-95, which was related to the STG-PSD-95 phase. As expected, the average number of STG proteins bound to one PSD-95 increased with increasing STG concentration (Figure 3C), whereas the number of STG proteins bound to PSD-95 decreased with the increasing concentration of GluN2B (Figure 3C). This is because GluN2B competes with STG with the same binding site on PSD-95. Consequently, the STG volume decreased in the high concentration range of GluN2B (Figure 3C). Of note, the competition between GluN2B and STG was nonlinear (gray dashed line in Figure 3C) and CaMKII-unbound GluN2B beads were bound more predominantly to PSD-95 at higher concentrations of GluN2B and STG (Figures 2C and 2F). The CaMKII and STG condensates were both required for the two-phase condensate because the two-phase region (Figure 2H) appeared only when the average number of GluN2B bound to one CaMKII was greater than 0.85 and the number of STG bound to one PSD-95 was greater than 0.41 (Figures 3E and S3).

Furthermore, PIP and partial engulfment were discriminated by the average ratio of PSD-95 bound to both GluN2B and STG (Figures 3F and 3G). The greater the number of PSD-95 bound to both GluN2B and STG, the more likely the appearance of PIP structures (Figures 3F and 3G), indicating that PSD-95 bridges the outer and inner phases. To explicate this phenomenon, we visualized the distribution of PSD-95 shared by GluN2B and STG that appeared at the interface between the inner and outer phases (shared PSD-95 in Figure 3H). In summary, PSD-95 played a role in the formation of the PIP structure by increasing the affinity between the two phases presumably by lowering their interfacial tension,  $\gamma_{\text{CaMKII,STG}}$ , at the macroscopic level (see STAR Methods).<sup>7,9–11,13,37</sup> The competitive binding-dependent phase transition between PIP and partial engulfment was also observed for RNA-binding proteins.<sup>8,11,12</sup>

We examined the effects of changes in the concentration of CaMKII and PSD-95 on the phase diagram (Figure S4). As CaMKII concentration increased, the PIP region expanded toward a higher concentration range of GluN2B (Figure S4A), suggesting that sequestration of GluN2B by CaMKII enabled STG to bind PSD-95 for PIP formation. The increase in PSD-95 resulted in the expansion of the STG and PIP regions (Figure S4B), which

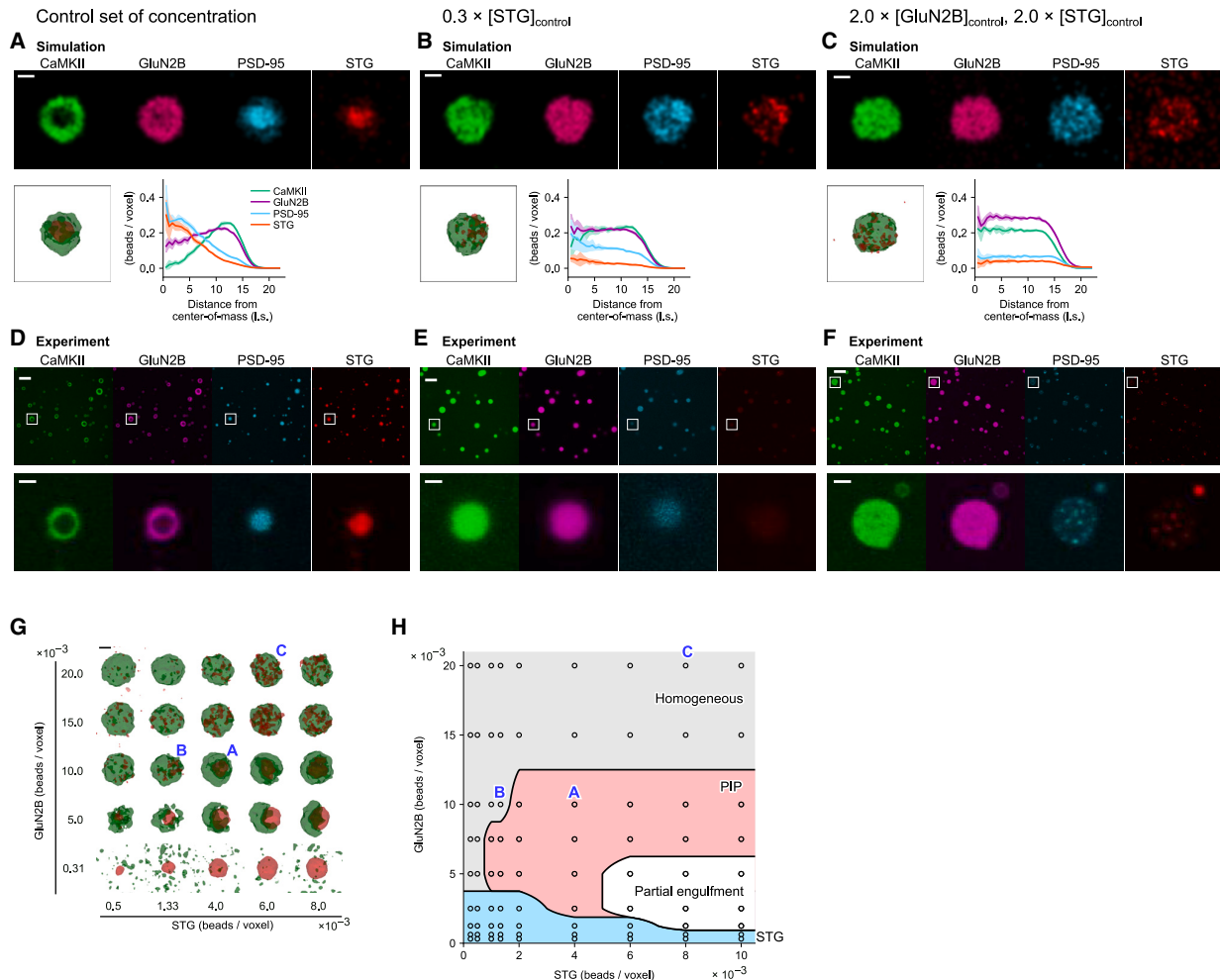


**Figure 2. Either PIP or homogeneous condensate appears depending on the protein concentration**

(A–C) Concentration dependence of LLPS in the MC simulation. The control set of concentrations was 10, 5, 5, and 1 (in  $\times 10^{-3}$  beads/voxel) for CaMKII, GluN2B, PSD-95, and STG, respectively. Top: cross-sectional concentration levels of indicated proteins. Scale bar, 10 l.s. Bottom left: a rendered shape of CaMKII and STG phases. The CaMKII-enriched region is colored green while the STG-enriched region is colored red. Bottom right: RDPs. (A) PIP structures appeared with the control set of concentrations.

(B) A homogeneous condensate appeared with a 3-fold decrease in STG concentration.

(C) A homogeneous condensate appeared with a simultaneous 2-fold increase in GluN2B and STG concentration.

(D–F) Experimentally observed condensates in the quaternary mixture of postsynaptic proteins. Top row: fluorescence microscopic images of proteins. Each protein was labeled with a unique-colored fluorescent dye. Bottom row: high-magnification images of an example condensate. (D) PIP structures appeared if the concentrations of CaMKII, GluN2B, PSD-95, and STG were 20, 5, 15, and 20  $\mu\text{M}$ , respectively. (E) A homogeneous condensate appeared with a 3-fold decrease in STG concentration. (F) A homogeneous condensate appeared with a simultaneous 2-fold increase in GluN2B and STG concentration. Scale bars, 5 and 1  $\mu\text{m}$  for low- and high-magnification images, respectively.

(G) Concentration-dependent shapes of LLPS. The cases (A)–(C) are indicated. All condensates were rotated so that CaMKII-enriched regions are located on the left side. Scale bar, 10 l.s.

(H) Phase diagram of the LLPS. Circles denote sampling points, and each colored region shares the same topological shape. Each region was determined based on visual inspection (see Figure S2A). Sampling points for cases (D)–(F) are indicated. STG (blue area) indicates monophasic condensation of STG and PSD-95, but not CaMKII or GluN2B. See Figure S2A.

may be due to the increasing amounts of GluN2B and STG binding to PSD-95. Taken together, competitive binding of STG and GluN2B was consistently important for PIP condensation.

Although PIP condensation was explained using site-specific interactions, IDR-mediated interactions also played important

roles in forming condensation (Figure S5). If the interactions through STG IDR were decreased to baseline, nearly all of the PIP region disappeared in the phase diagram (Figures S5B and S5C). This may occur because the STG condensation became looser and the surface tension of the STG phase,  $\gamma_{\text{STG}}$ , became

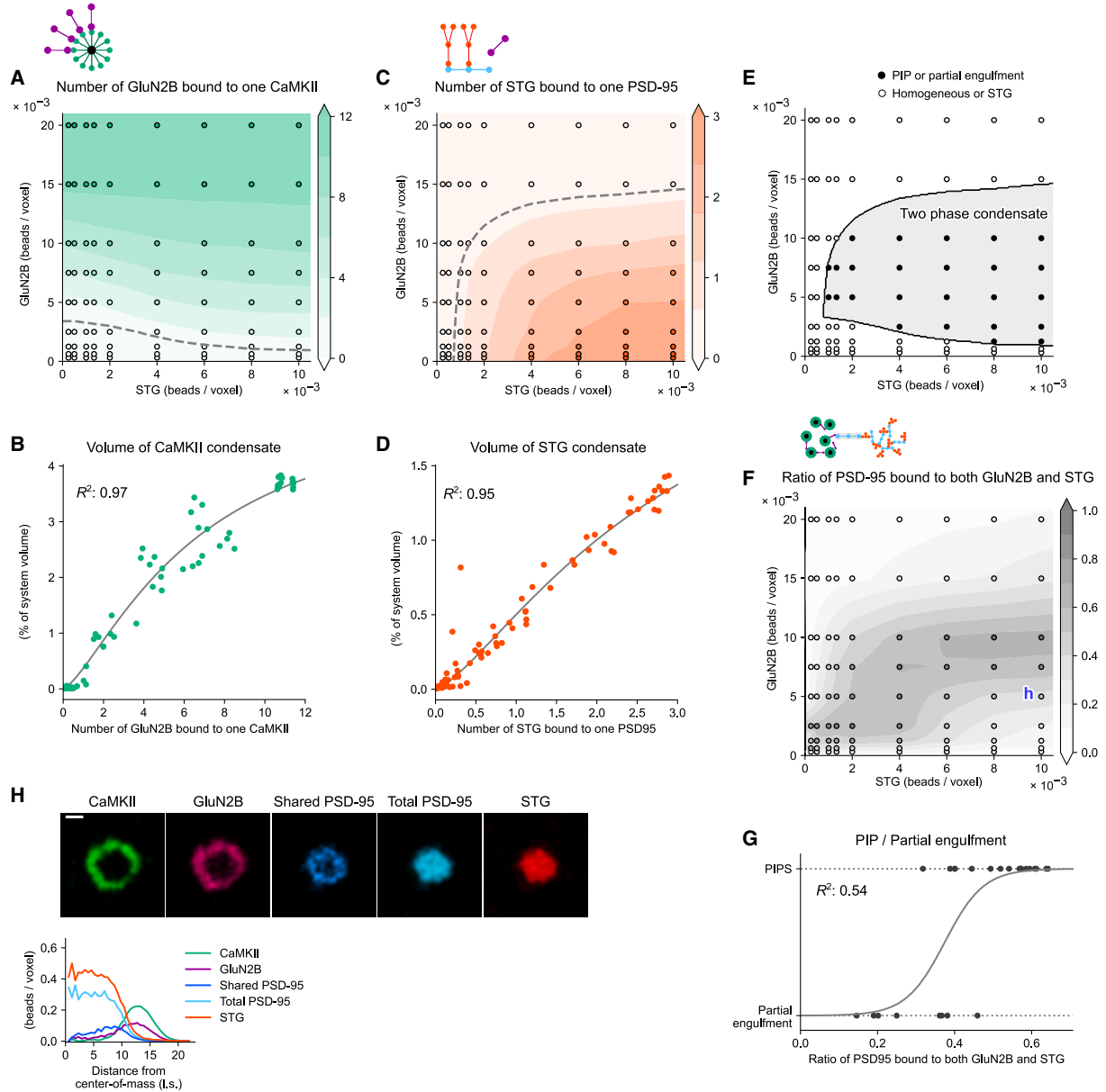


**Figure 3. The concentration dependence of two-phase LLPS is explained by competitive binding**

(A) Average number of GluN2B proteins bound to one CaMKII protein were plotted under the various STG and GluN2B concentrations. Open circles indicate the observation while colored areas show their linear interpolation.

(B) The GluN2B-CaMKII binding explains the volume of CaMKII condensate. Volumes of the largest CaMKII condensate were plotted against average numbers of GluN2B-CaMKII binding in the system. The Hill function was fitted, and the goodness-of-fit ( $R^2$ ) is shown.

(C) The average number of STG proteins bound to one PSD-95 in the same concentration space of STG and GluN2B.

(D) The STG-PSD-95 binding explains the volume of STG condensate. Volumes of the largest STG condensate were plotted against average numbers of STG-PSD-95 binding. The Hill function was fitted.

(E) The two-phase separation is explained by two types of binding. The gray-shaded area, which was derived from equivalent lines of average binding in (A) and (C) (see gray dashed lines) covered the two-phase separation with 100% accuracy. The procedure is shown in Figure S3.

(F) Ratios of PSD-95 sharing by GluN2B and STG in the condensates.

(legend continued on next page)

lower (see STAR Methods). Similarly, the homogeneous condensates largely disappeared because STG was not trapped by the condensate (Figures S5B, S5C, and S5D). Thus, site-specific and IDR-mediated interactions are both important for the reproduction of experimentally observed LLPS.

### PIP formation depends on linker length and multivalency of CaMKII

Next, we examined the role of the unique dodecameric structure of CaMKII in the PIP organization. Here, protein concentrations were fixed including the concentration of CaMKII-binding beads despite the change in the CaMKII valency. When the valency of CaMKII was decreased from 12 to 4, the PIP organization disappeared, and a homogeneous condensate appeared instead (Figures 4A and 4B). Decreasing the valency of CaMKII further to 2 caused the CaMKII to dissipate, and the remaining GluN2B, PSD-95, and STG formed a homogeneous condensate (Figure 4C). High valency was found to be essential for condensation as demonstrated in a previous computational study.<sup>49,50</sup> The condensates were stably separated into two phases if CaMKII had more than six valencies (Figures 4E and 4F). This suggests that only one side of the double hexamer CaMKII is sufficient to form a two-phase condensate. Phase separation of the synaptic proteins occurs within the limited spaces at PSD. If one hexamer of CaMKII faces the PSD and binds to proteins, such as GluN2B, the other hexamer is oriented away from the PSD and likely binds to soluble proteins to trap them in a manner dependent upon  $\text{Ca}^{2+}/\text{CaM}$ , thereby working as a  $\text{Ca}^{2+}/\text{CaM}$ -dependent postsynaptic clustering mechanism.<sup>35</sup>

We then tested the effect of the overall size of CaMKII protein by changing the linker length. When the CaMKII linker length was increased, two-phase condensates still appeared, but their shape was due to partial engulfment rather than PIP (Figure 4D). This trend was consistently observed at a valency between 6 and 12, and the longer linker length favored the partial engulfment (Figure 4E). Interestingly, the linker-length dependence was observed only for CaMKII, but not for other proteins (Figure 5). The valency and linker-length dependence of CaMKII in LLPS is summarized in the phase diagram (Figures 4F and S2B), which showed that the valency and linker length independently affected LLPS (Figure 4F), although both had a significant effect on the LLPS without changing any other parameters, such as the concentration and binding energies.

### The shorter the CaMKII linker, the lower the surface tension of the condensate

Although the simultaneous binding of PSD-95 with GluN2B and STG was required for PIP in the case of concentration dependence (Figures 2 and 3F–3H), the ratio of PSD-95 bound to both GluN2B and STG did not change with the CaMKII linker length (Figure S6C), suggesting that another mechanism contributed to the phase transition between PIP and partial engulfment. The capillary theory demonstrates that both interfacial and sur-

face tensions govern this type of phase transition.<sup>7,9–11,13,37</sup> In this study, through cohesive force, we associated CaMKII linker length with the surface tension of the CaMKII-GluN2B phase.

Considering the difficulty of examining the surface tensions of the two-phase condensate, we simulated the binary mixtures of CaMKII and GluN2B and examined the spherical condensates (Figures 6A, 6B, and S7A). We first found that the CaMKII hub with a longer linker length (6 l.s.) accumulated at the boundary region of the condensate than of the CaMKII hub with a short linker (3 l.s.) (Figures 6A and 6B, top). The binding beads (kinase domain) of CaMKII at the border were not inwardly directed to the condensate center but radiated evenly from the center hub (Figures 6A and 6B, bottom, and Figure S7B). The radiation of binding beads may produce a surface tension under more realistic conditions.

Therefore, we derived the putative inward force produced by the CaMKII-binding beads. In the current setup of MC simulation, the CaMKII linker had no tension associated with macroscopic properties. Nevertheless, the CaMKII binding beads could not move beyond a predetermined linker length from the center hub, and this spatial confinement can be considered as contraction force toward the center hub. This contraction force may partly be directed toward the center of the condensate and thus the inward cohesive force, whereas the tangential forces are canceled out under the spherical symmetry.

Based on this idea, we calculated the angle  $\theta_i$  between the linker  $i$  direction and the center of mass of a target condensate (Figures 6C–6E).  $\theta_i$  corresponds to the direction of linker-generated force with respect to the center of a condensate and showed a weak bias toward zero degrees if the CaMKII linker length was 3 l.s. (Figure 6D, bottom). By contrast, if the CaMKII linker length was 6 l.s., the distribution of  $\theta_i$  was more concentrated at zero degrees (Figure 6E). If the linker produces a contraction force, the component of this force directed to the center (cohesion force) can be calculated as  $\cos(\theta_i)$ . The averaged component,  $\overline{\cos(\theta)}$ , showed a clear difference between the linker lengths of 3 and 6 l.s. (Figure 6F).

Effective contraction events of a linker occur when this is nearly fully stretched. Furthermore, if the total cohesion force toward the center is divided by the circumference length  $2\pi r$ , this corresponds to the surface tension.<sup>51</sup> Therefore, we derived the putative surface tension  $\gamma$  and confirmed that the difference in  $\overline{\cos(\theta)}$  was preserved (Figures 6F and 6G). In the plane of valency and linker length, the lower surface tension  $\gamma$  occupied the PIP region (Figures 4F and 6H), the higher surface tension  $\gamma$  occupied the partial engulfment (Figures 4F and 6H), and the surface tension  $\gamma$  explained this phase transition ( $R^2 = 0.82$ , Figure 6I).

In capillary theory, the surface tension,  $\gamma_{\text{STG}}$  and  $\gamma_{\text{CaMKII}}$ , and interfacial tension  $\gamma_{\text{CaMKII,STG}}$  determine the contact angle of two immiscible liquids and their topological characteristics (STAR Methods).<sup>7,11,37,52</sup> For the transition between PIP and partial engulfment, the PIP appears if  $\gamma_{\text{STG}} > \gamma_{\text{CaMKII}} + \gamma_{\text{CaMKII,STG}}$

(G) The PSD-95 sharing ratio in (F) discriminates the PIP and partial engulfment. Shape data were taken from Figure 2H. Efron's  $R^2$  is displayed as a measure of the goodness-of-fit of the logistic function.

(H) The sharing of PSD-95 appears at the interface region between the CaMKII and STG phases. The concentrations are indicated in (F). For visibility, the RDP was generated only from the last time frame data. Scale bar, 10 l.s.

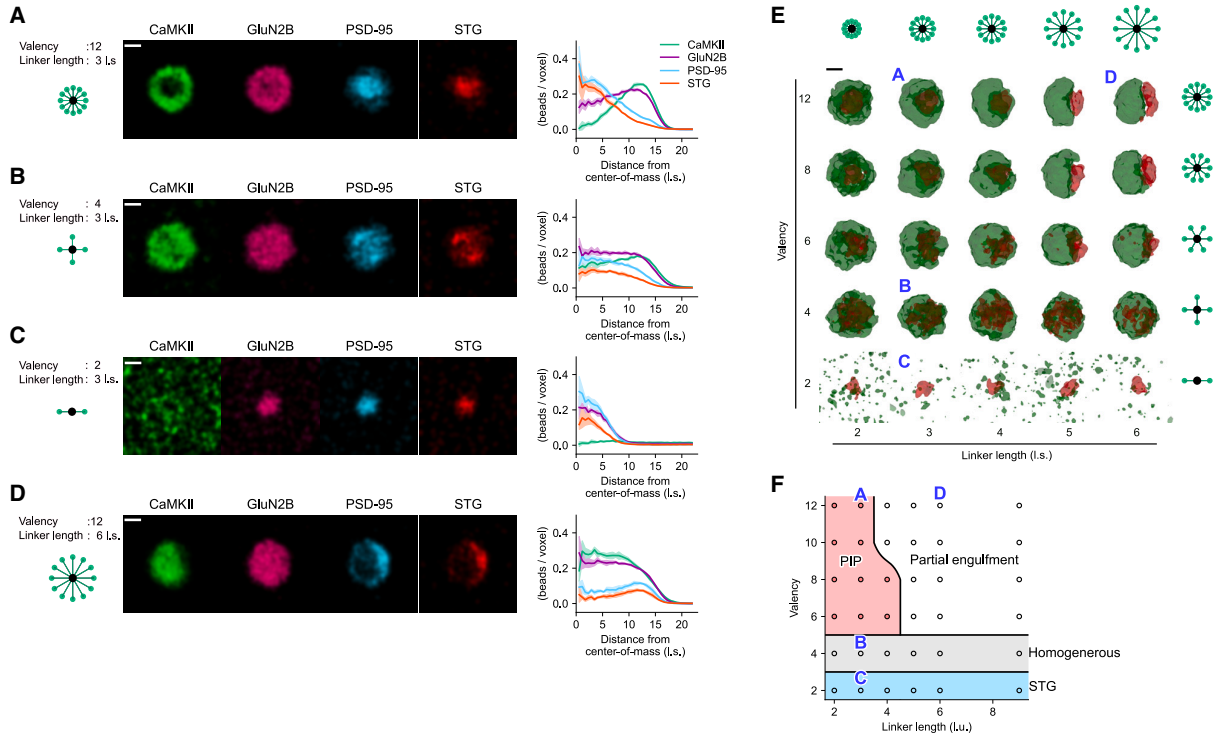


**Figure 4. The PIP formation depends on both the valency and linker length of CaMKII**

(A) The PIP formation under the standard CaMKII shape. CaMKII had 12 binding beads with a linker length of 3 l.s. Left: schematics; center: cross-sectional levels of constituent proteins; right: RDPS.

(B) A homogeneous condensate formed if CaMKII had a valency of 4.

(C) A homogeneous condensate of GluN2B-PSD-95-STG formed if CaMKII had a valency of 2.

(D) A partially engulfed condensate formed if CaMKII had a linker length of 6 l.s.

(E) The valency and linker-length dependence of two-phase condensates. Condensates in (A)–(D) are indicated.

(F) Phase diagram of the LLPS. This phase diagram was determined based on Figure S2B. Scale bar, 10 l.s. See Figure S2B.

(Figure 6J, left), and the partial engulfment appears if  $\gamma_{STG} < \gamma_{CaMKII} + \gamma_{CaMKII,STG}$  (Figure 6J, right). The derived  $\gamma$  constitutes a portion of  $\gamma_{CaMKII}$ . Note that  $\gamma$  was not equal to the total  $\gamma_{CaMKII}$ , because  $\gamma_{CaMKII}$  includes the surface tension resulting from GluN2B (Figure 6J).

Although it is difficult to calculate  $\gamma_{STG}$  and  $\gamma_{CaMKII,STG}$ , they were both considered similar regardless of the CaMKII linker length, because a similar number of STG was bound to one PSD-95 (Figure S6B) and a similar number of PSD-95 was bound to both GluN2B and STG (Figure S6C). Under the constant  $\gamma_{STG}$  and  $\gamma_{CaMKII,STG}$ ,  $\gamma_{CaMKII}$ , which was affected by the linker length of CaMKII, explains the phase transition. Therefore,  $\gamma_{CaMKII}$  is likely responsible for the phase transition.

#### Modular networks in the CaMKII-GluN2B condensates

The simulation time required to form the stable CaMKII-GluN2B condensate was dependent on the shape of CaMKII. To quantify this time, we mimicked a fluorescence recovery after photobleaching assay on the CaMKII-GluN2B condensates (STAR Methods; Figures 7A–7C). For this simulation, we used only local MC moves and considered the number of these as a proxy for time.<sup>40</sup> The recovery rate of CaMKII in the photobleached region

was 5-fold slower if the CaMKII had a short linker length (Figures 7A and 7B). This slow rate was not derived from the longer lifetime of each CaMKII-GluN2B binding (Figure S7), the higher condensate concentration that may prevent the CaMKII movement (Figure S8), or the slow movement of independent CaMKII (Figure S9), but from their clustering connections (Figures 7D–7F). Herein, each GluN2B-mediated CaMKII-CaMKII connection (CaMKII-GluN2B-CaMKII connection) was considered as a unit CaMKII-CaMKII connection, and the connectivity of the simplified CaMKII network was quantified using the clustering coefficient (CC) (Figure 7D; STAR Methods).<sup>53</sup> The CC counts the number of connections between the neighboring CaMKII proteins to show the density of connections around the target CaMKII (Figure 7D). The CC averaged over the target condensate explained the slowdown of CaMKII movement almost completely ( $R^2 = 0.80$ , Figures 7C, 7E, and 7F). The high CC presumably caused a higher rejection rate of local MC moves to produce the slow movement of CaMKII. Note that the MC moves differ from the real-time development as the MC simulation does not incorporate any diffusion rate constants or forward/backward-binding rate constants. Nevertheless, the cluster formation should also produce the slow diffusion of

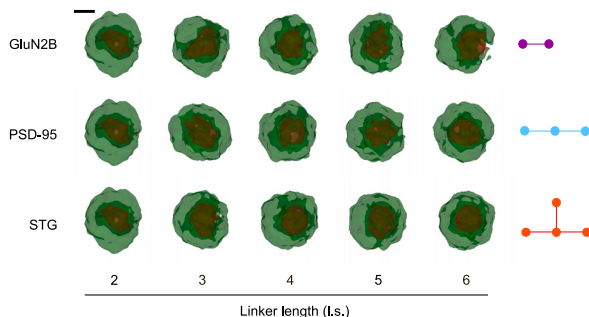


**Figure 5.** PIP formation is independent of the linker length of GluN2B, PSD-95, and STG. Rendered shapes of CaMKII and STG phases were plotted if the linker length of GluN2B, PSD-95, or STG was changed between 2 and 6 l.s. Scale bar, 10 l.s.

CaMKII in more realistic situations because the coupled CaMKII should have the larger Stokes radius. This has been demonstrated in MD simulation.<sup>54,55</sup> The CaMKII with a short linker length and high valency is likely to show slow diffusion in the condensate due to its local clustering.

The averaged CC only characterized the local connectivity. We further examined the more global characteristics of connectivity in the CaMKII-GluN2B condensates. In this analysis, we again targeted the GluN2B-mediated CaMKII connections and considered each CaMKII-GluN2B-CaMKII connection as a unit CaMKII-CaMKII connection (Figures 7G and 7H). The simplified CaMKII network was analyzed using the Girvan-Newman algorithm, a hierarchical community detection method. The CaMKII connection exhibiting the highest edge-betweenness centrality was first selected and then removed. The repeats of this selection-removal cycle progressively decomposed the CaMKII network into multiple subnetworks whose CaMKII proteins were more densely connected (dendrograms in Figures 7G and 7H). This decomposition revealed that CaMKII with the short linker had a more modular network, i.e., the CaMKII-GluN2B condensate comprised multiple subnetworks of several dozen CaMKII proteins (Figure 7G). Conversely, CaMKII with the long linker had a smoother and more homogeneous network in the condensate (Figure 7H). When the modularity was introduced as a measure of this global connectivity (STAR Methods), the CaMKII-GluN2B condensates that had CaMKII with a short linker showed a large modularity if CaMKII had a valency  $>8$  (Figure 7I). If the CaMKII valency was  $<6$  l.s., this trend disappeared, presumably because the low valency CaMKII made many smaller subnetworks regardless of the linker length.

The modularity and averaged CC are different concepts (Figures 7E and 7I): the modularity compares the relative number of intermodular connections against the background intramodular connections, whereas the CC quantifies the absolute degree of clustering in the network (STAR Methods). The modular structure of CaMKII proteins always appeared when a short linker length was present, and the higher valency further slowed the movement of CaMKII. Such dynamic cluster formation and the associated slowdown of protein diffusion have been demonstrated in MD simulation.<sup>54,55</sup>

## DISCUSSION

Herein, we sought to elucidate the intrinsic factors that determine the topology of a two-phase condensate and developed a minimalistic computational model comprising four postsynaptic proteins. The quaternary mixture reproduced a form of two-phase condensates, termed PIP. The PIP did not always appear and, depending on the concentrations of constituent proteins, the mixture showed homogeneous or partially engulfed condensation, the former of which was experimentally validated. Model analyses dissected the underlying physicochemical forces that drove these forms of condensates. The CaMKII showing PIP had a high valency and short linker length, and such a CaMKII condensate exhibited a low surface tension, modular structure, and consequently slow diffusion.

Interestingly, those characteristics of CaMKII (i.e., low surface tension, modular structure, and slow diffusion) are aligned with the required functions of CaMKII as a synaptic memory unit. In principle, LLPS shows poor stability.<sup>17,18</sup> The continued growth of condensates may occur because of the absorption/sequestration of small condensates located in small domains, such as dendritic spines, which harbor the postsynaptic structures.<sup>56,57</sup> Contrary to this process, synaptic condensates need to remain in place long enough to perform their functions. Theories for the coalescence process indicate that low surface tension and slow diffusion are both required for the long lifetime of small condensates.<sup>56,58</sup> The shape characteristics of CaMKII lead to low surface tension and slow diffusion to ensure persistence for an extended period. The longer lifetime of the CaMKII condensates is important to activate downstream signaling for synaptic plasticity or synaptic tags.<sup>35,59</sup> In addition to PSD-95 anchoring the GluN2B-CaMKII condensate at PSD, the CaMKII shape might underlie the stability of small condensates in small postsynaptic domains. Note that other mechanisms that regulate condensate size have also been reported.<sup>18,60</sup> Small condensates with a diameter less than 100 nm are dominant in some cell types.<sup>61</sup>

For consistency with the preceding study,<sup>16</sup> we introduced GluN2B to form the CaMKII condensate. However, other client proteins, such as Shank3<sup>62</sup> and Tiam1,<sup>63,64</sup> are known to bind CaMKII together and may form CaMKII condensate. Also, CaMKII alone forms condensate at low pH<sup>65,66</sup> The characteristic shape of CaMKII is well conserved across metazoans.<sup>67</sup> The role of CaMKII condensate may not be restricted to the nanocolumn formation at PSD<sup>16</sup> and the CaMKII condensate may play more universal roles in the formation of synaptic memory, thus synaptic plasticity.

The concentration dependence of LLPS revealed that the competitive binding of STG and GluN2B to PSD-95 was important for the PIP formation. Homogeneous condensation occurred at the high GluN2B concentrations (Figures 2G and 2H) because PSD-95 was fully occupied with the excess amount of GluN2B, and the PSD-95-GluN2B complex further interacted with CaMKII to form the CaMKII-GluN2B-PSD-95 condensate (Figures S1D–S1F),<sup>44</sup> whereas STG remained associated because of the STG-dependent IDR-mediated interactions (Figure S5). Similar competitive binding was observed in the two-phase separation of RNA and RNA-binding proteins.<sup>11,12</sup> Thus,

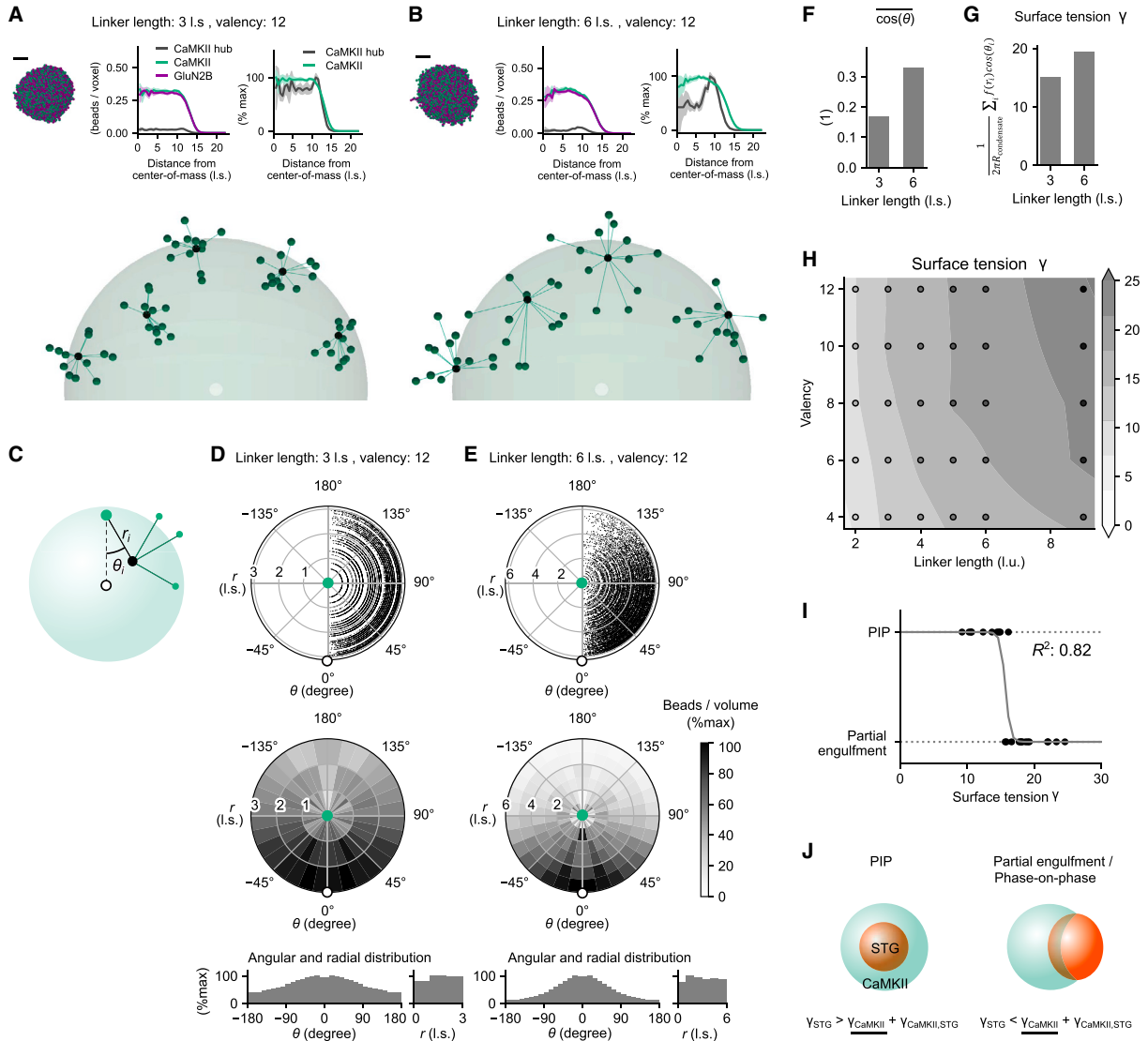


**Figure 6. The analysis of CaMKII-GluN2B condensates explains the surface tension-dependent transition of a two-phase condensate**

(A) The mixture of CaMKII and GluN2B formed a spherical-shaped condensate (left, top row), enabling numerical analyses of putative surface tension. RDPs of CaMKII hub, CaMKII-binding beads (denoted as CaMKII), and GluN2B (center and right, top row) and the example sampling of CaMKII (bottom row) are also shown. Five CaMKII proteins were sampled to show spatial arrangements (condensate radius: 13.0 l.s.; Figure S6B, center).

(B) Same as (A), but the linker length of CaMKII was 6 l.s. Four CaMKII proteins were sampled at the bottom (condensate radius: 12.7 l.s.; Figure S6B, right).

(C–E) Spatial distribution of the CaMKII hub beads (black points on the left) when the tethering binding beads were centered (green points); two standard cases are shown (D) and (E). Angles of the linker  $i$  versus the binding bead-condensate center axis ( $\theta_i$ ) were obtained as well as the distances between each CaMKII hub and binding bead ( $r_i$ ) (C); scatterplots showing the polar coordinates (top rows in D and E). The polar (middle rows), angular (bottom rows, left), and radial distributions (bottom rows, right) are also shown. Levels in the polar distribution were normalized by the segmented volumes and those in the angular distribution were normalized by the segmented area.

(F) Averaged cosine angles for the two cases.

(G) Effective surface tension  $\gamma$  defined by  $\sum_i f(r_i) \cos(\theta_i) / 2\pi R_{\text{condensate}}$  (STAR Methods).

(H) The surface tension  $\gamma$  in the plane of valency and linker length.

(I) The surface tension  $\gamma$  explains the transition between PIP and partial engulfment. Efron's  $R^2$  is displayed as a goodness of fit of the logistic regression.

(J) Macroscopic determinant of the PIP and partial engulfment. The shape of the two-phase condensate is determined by the surface tension of the STG-PSD-95 phase,  $\gamma_{STG}$ , and the CaMKII-GluN2B phase,  $\gamma_{CaMKII}$ , and their interfacial tension,  $\gamma_{CaMKII,STG}$ . The calculated  $\gamma$  should be a part of  $\gamma_{CaMKII}$ . See Figure S7.

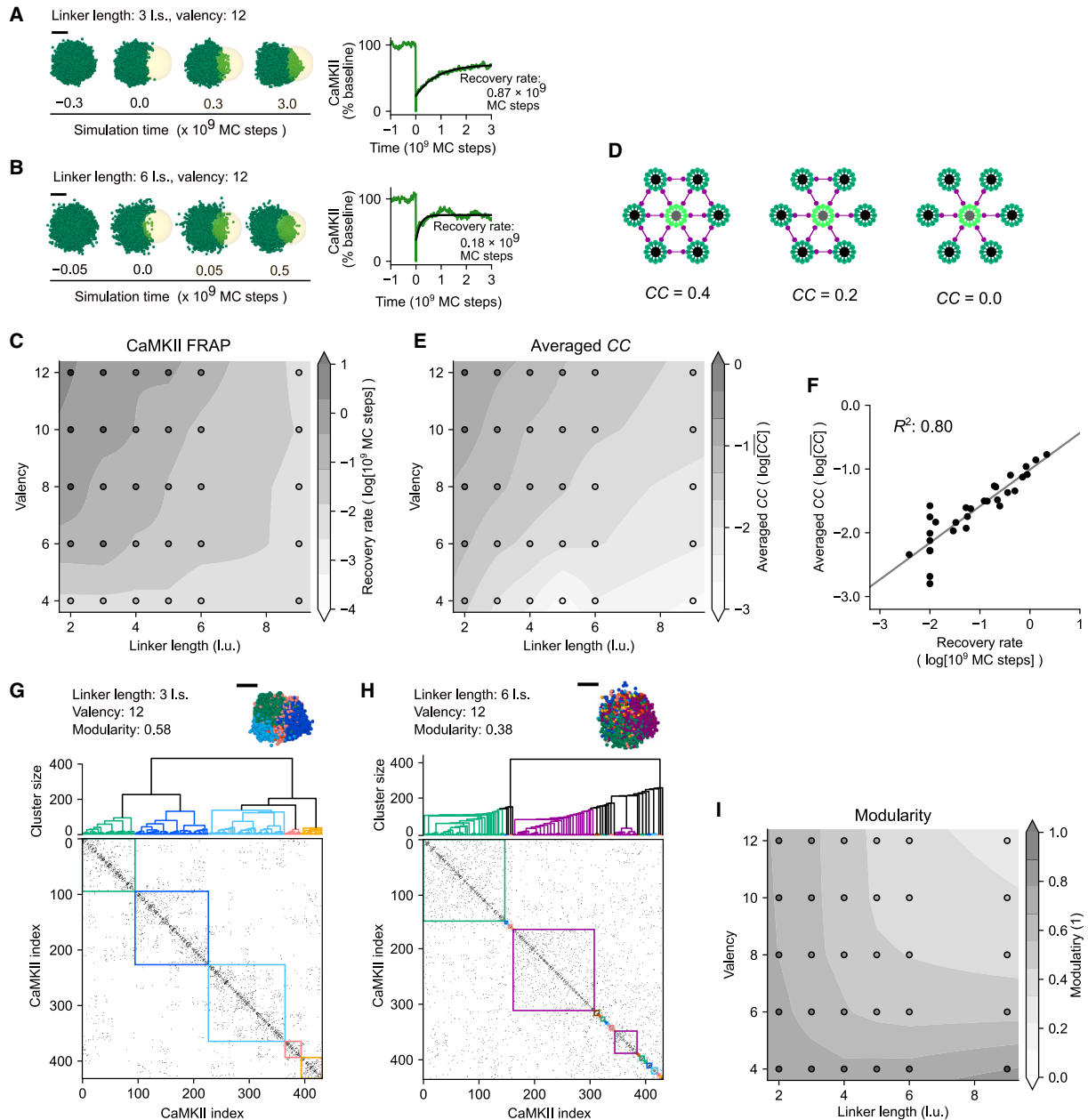


**Figure 7. Recovery of CaMKII from the photobleaching correlates with the condensate network**

(A) A fluorescence recovery after photo bleaching (FRAP) experiment was mimicked on the CaMKII-GluN2B condensates (CaMKII linker length: 3 l.s., valency: 12; left). At the 0 MC step, a part of the CaMKII condensate (yellow spherical region; radius: 8.7 l.s.) was made invisible, and then the recovery rate at this region was quantified (right). Scale bar, 10 l.s.

(B) Same as (A), but the linker length of CaMKII was 6 l.s.

(C) Recovery rates in the plane of valency and linker length.

(D) Clustering coefficient (CC) for the characterization of connectivity in the CaMKII-GluN2B condensates (see STAR Methods). In the condensate, CaMKII proteins (green) were bound to other CaMKII proteins via GluN2B (purple). If a target CaMKII protein (highlighted in purple) that have six surrounding connections ( $n_{edge} = 6$ , left case), this gives  $CC = 2n_{edge}/N(N - 1) = 0.4$ . If  $N = 6$  and  $n_{edge} = 3$ , this gives  $CC = 0.2$  (center case), and if  $N = 6$  and  $n_{edge} = 0$ , this gives  $CC = 0.0$  (right case). In general, the larger CC denotes a denser local connectivity.

(E) Averaged CC for all CaMKII proteins in the condensate.

(F) The FRAP recovery rate is explained by the averaged CC.  $R^2$  is displayed as a goodness of fit of a linear function.

(legend continued on next page)

the competitive binding should be a motif in the formation of multiphase condensates.

The analyses of surface tension clarified that the directions of the CaMKII linkers were biased toward the center of condensate if the linker length was long (Figures 6C–6E). This was partly because the long linker length became closer in size to the condensate radius (Figures 6A and 6B). The surface accumulation of CaMKII with a longer linker presumably minorly affected the surface tension. In a larger and open system, the surface accumulation of CaMKII would be a dominant factor with high surface tension because the summed cohesive force of CaMKII only at the surface region corresponds to the surface tension. Although the impact of the linker length on LLPS formation has been previously investigated,<sup>27,29</sup> no study has yet provided systematic insights into how linker length controls the condensate shape. Herein, we successfully connected the microscopic linker length of CaMKII with the macroscopic forms of LLPS.

Our approach can easily be extended to incorporate many other postsynaptic proteins.<sup>5,42,68–70</sup> Furthermore, our simulation can be extended to understand the other multiphasic LLPS that are based on divergent structures such as pentameric nucleophosmin (NPM1) in the nucleolus,<sup>7</sup> Rubisco holoenzymes-EPYC1 condensate in pyrenoid,<sup>27</sup> and Polycomb-repressive complex 1 (PRC1) family complexes in chromatin organization.<sup>31,32</sup> Their unique forms would also be realized by the interfacial tensions of constituent molecules.<sup>7,10,11,13</sup> The manipulation of the CaMKII linker length had drastic impacts on the multiphasic LLPS. Similar manipulations may be useful to control multiphasic LLPS in such systems.

#### Limitations of the study

In this study, the quaternary mixture of postsynaptic proteins was simulated in a 3D space to be compatible with LLPS in *in vitro* experiments. However, these proteins should form LLPS in a 2D space under postsynaptic membranes *in vivo*. Thus, it will be interesting to perform the same simulation in a 2D space. Yamada et al. performed such a 3D-2D conversion simulation and found that the STG-PSD-95 condensate in the 2D space was more unstable compared with that in the 3D space.<sup>47</sup> Thus, the study of such dimensionality is an important future direction, particularly when considering the appearance of many forms of LLPS in 2D spaces.<sup>71</sup>

**Q9** A recent study by Cai et al. showed that short linker CaMKII $\alpha$ , but not long linker CaMKII $\beta$ , forms condensates with GluN2B.<sup>48</sup> This trend was not observed in the present simulation (e.g., Figure S7A). Presumably, this difference resulted from different experimental setups. Unlike the experiment that we replicated,<sup>16</sup> Cai et al. used the full-length carboxyl tail of GluN2B, which contained two CaMKII interaction sites,<sup>46</sup> and did not use the oligo-

meric form of GluN2B. This difference in GluN2B may have caused the loss of the CaMKII $\beta$  condensate, although the mechanisms remain unclear. More detailed protein modeling may provide insight into the functional consequences of different CaMKII and GluN2B.

We found that the CaMKII linker length was a determinant of condensate shape (i.e., PIP and partial engulfment; Figure 4). Also, CaMKII with a short linker exhibited a modular structure in CaMKII-GluN2B condensates (Figure 7G). One may think that the modular structure affects condensate shape considering that the modularity (Figure 7I) exhibited a similar trend with condensate shape (Figure 4F); however, the CaMKII-GluN2B condensates exhibited spherical shapes regardless of the modular structure (Figures 7G and S7A). Whether and how CaMKII modularity affects condensate shape remains unclear. More sophisticated methods for calculating local surface tension are likely required to address this question.

#### RESOURCE AVAILABILITY

##### Lead contact

Requests for further information, resources, and reagents should be directed to and will be fulfilled by the lead contact, Hidetoshi Urakubo ([hurakubo@gmail.com](mailto:hurakubo@gmail.com)).

##### Materials availability

This study did not generate new unique reagents.

##### Data and code availability

- All data reported in this paper are available upon request from the lead contact.
- The code used for modeling and simulation, as well as for analyses and visualization, have been deposited at GitHub and are publicly available as of the date of publication. The GitHub sites and DOIs are listed in the [key resources table](#).
- Any additional information required to reanalyze the data reported in this paper is available from the lead contact upon request.

#### ACKNOWLEDGMENTS

We thank F. Dar and R.V. Pappu for providing us with the updated version of the LaSSI simulation engine. This project received funding from the Core Research for Evolutional Science and Technology (CREST), the Japan Science and Technology Agency (JST) (grant no. JPMJCR20E4) to T.H., Y.H., and H.U. T.H. is supported by JSPS KAKENHI (JP19K06885), Kobayashi foundation, and ISHIZUE2024 of Kyoto University. Y.H. is supported by Grant-in-Aid for Scientific Research JP18H05434, JP20K21462, and JP22K21353 from the MEXT, Japan; the Uehara Memorial Foundation; the Naito Foundation; Research Foundation for Opto-Science and Technology; Novartis Foundation; the Takeda Science Foundation; and HFSP Research Grant RGP0020/2019. H.U. is supported by JSPS KAKENHI (JP24H02317 and JP20K12062).

**Q10**

(G) Adjacency matrix of CaMKII connections (CaMKII linker length: 3 l.s.; bottom). Each CaMKII connection via GluN2B is represented by a dot in the matrix. The order of CaMKII proteins was sorted using a hierarchical method for community detection (Girvan-Newman algorithm; see STAR Methods). Hierarchical communities are shown in the dendrogram (top), and clusters were colored below the threshold where 150 CaMKII proteins were assigned to the largest cluster. The shape of the condensate is shown (top, right). Scale bar, 10 l.s.

(H) Same as (G), but the linker length of CaMKII is 6 l.s.

(I) The values of the measure “modularity” in the plane of valency and linker length (STAR Methods). See Figures S8–S10.

## AUTHOR CONTRIBUTIONS

V.P. and H.U. designed the research. V.P., H.U., and T.H. performed the research. V.P. and H.U. analyzed the data. H.U. and Y.H. supervised the research. All authors wrote the manuscript.

## DECLARATION OF INTERESTS

The authors declare no competing interests.

## STAR★METHODS

Detailed methods are provided in the online version of this paper and include the following:

- [KEY RESOURCES TABLE](#)
- [EXPERIMENTAL MODEL AND STUDY PARTICIPANT DETAILS](#)
  - Bacterial strain
- [METHOD DETAILS](#)
  - *In vitro* phase separation experiment
  - LaSSI simulation
  - Linker length
  - Binding energy
  - Simulation time schedule
- [QUANTIFICATION AND STATISTICAL ANALYSIS](#)
  - Visualization
  - Surface tension
  - Surface tension and topology of a two-phase condensate
  - Connectivity analyses
  - Graph theoretical analyses

## SUPPLEMENTAL INFORMATION

Supplemental information can be found online at <https://doi.org/10.1016/j.celrep.2025.115504>.

Received: September 17, 2024

Revised: February 5, 2025

Accepted: March 12, 2025

## REFERENCES

1. Mohanty, P., Kapoor, U., Sundaravadivelu Devarajan, D., Phan, T.M., Rizuan, A., and Mittal, J. (2022). Principles governing the phase separation of multidomain proteins. *Biochemistry* *61*, 2443–2455. <https://doi.org/10.1021/acs.biochem.2c00210>.
2. Holehouse, A.S., and Kragelund, B.B. (2024). The molecular basis for cellular function of intrinsically disordered protein regions. *Nat. Rev. Mol. Cell Biol.* *25*, 187–211. <https://doi.org/10.1038/s41580-023-00673-0>.
3. Roden, C., and Gladfelter, A.S. (2021). RNA contributions to the form and function of biomolecular condensates. *Nat. Rev. Mol. Cell Biol.* *22*, 183–195. <https://doi.org/10.1038/s41580-020-0264-6>.
4. Shin, Y., and Brangwynne, C.P. (2017). Liquid phase condensation in cell physiology and disease. *Science* *357*, eaaf4382. <https://doi.org/10.1126/science.aaf4382>.
5. Chen, X., Wu, X., Wu, H., and Zhang, M. (2020). Phase separation at the synapse. *Nat. Neurosci.* *23*, 301–310. <https://doi.org/10.1038/s41593-019-0579-9>.
6. Banani, S.F., Lee, H.O., Hyman, A.A., and Rosen, M.K. (2017). Biomolecular condensates: organizers of cellular biochemistry. *Nat. Rev. Mol. Cell Biol.* *18*, 285–298. <https://doi.org/10.1038/nrm.2017.7>.
7. Feric, M., Vaidya, N., Harmon, T.S., Mitrea, D.M., Zhu, L., Richardson, T.M., Kriwacki, R.W., Pappu, R.V., and Brangwynne, C.P. (2016). Coexisting liquid phases underlie nucleolar subcompartments. *Cell* *165*, 1686–1697. <https://doi.org/10.1016/j.cell.2016.04.047>.
8. Kim, T.H., Tsang, B., Vernon, R.M., Sonenberg, N., Kay, L.E., and Forman-Kay, J.D. (2019). Phospho-dependent phase separation of FMRP and CAPRIN1 recapitulates regulation of translation and deadenylation. *Science* *365*, 825–829. <https://doi.org/10.1126/science.aax4240>.
9. Feric, M., Sarfallah, A., Dar, F., Temiakov, D., Pappu, R.V., and Misteli, T. (2022). Mesoscale structure-function relationships in mitochondrial transcriptional condensates. *Proc. Natl. Acad. Sci. USA* *119*, e2207303119. <https://doi.org/10.1073/pnas.2207303119>.
10. Fei, J., Jadalilha, M., Harmon, T.S., Li, I.T.S., Hua, B., Hao, Q., Holehouse, A.S., Reyer, M., Sun, Q., Freier, S.M., et al. (2017). Quantitative analysis of multilayer organization of proteins and RNA in nuclear speckles at super resolution. *J. Cell Sci.* *130*, 4180–4192. <https://doi.org/10.1242/jcs.206854>.
11. Kaur, T., Raju, M., Alshareedah, I., Davis, R.B., Potoyan, D.A., and Banerjee, P.R. (2021). Sequence-encoded and composition-dependent protein-RNA interactions control multiphasic condensate morphologies. *Nat. Commun.* *12*, 872. <https://doi.org/10.1038/s41467-021-21089-4>.
12. Lin, A.Z., Ruff, K.M., Dar, F., Jalihal, A., King, M.R., Lalmansingh, J.M., Posey, A.E., Erkamp, N.A., Seim, I., Gladfelter, A.S., and Pappu, R.V. (2023). Dynamical control enables the formation of demixed biomolecular condensates. *Nat. Commun.* *14*, 7678. <https://doi.org/10.1038/s41467-023-43489-4>.
13. Rana, U., Xu, K., Narayanan, A., Walls, M.T., Panagiotopoulos, A.Z., Avalos, J.L., and Brangwynne, C.P. (2024). Asymmetric oligomerization state and sequence patterning can tune multiphase condensate miscibility. *Nat. Chem.* *16*, 1073–1082. <https://doi.org/10.1038/s41557-024-01456-6>.
14. Fare, C.M., Villani, A., Drake, L.E., and Shorter, J. (2021). Higher-order organization of biomolecular condensates. *Open Biol.* *11*, 210137. <https://doi.org/10.1098/rsob.210137>.
15. Hirose, T., Ninomiya, K., Nakagawa, S., and Yamazaki, T. (2023). A guide to membraneless organelles and their various roles in gene regulation. *Nat. Rev. Mol. Cell Biol.* *24*, 288–304. <https://doi.org/10.1038/s41580-022-00558-8>.
16. Hosokawa, T., Liu, P.W., Cai, Q., Ferreira, J.S., Levet, F., Butler, C., Sibarita, J.B., Choquet, D., Groc, L., Hossy, E., et al. (2021). CaMKII activation persistently segregates postsynaptic proteins via liquid phase separation. *Nat. Neurosci.* *24*, 777–785. <https://doi.org/10.1038/s41593-021-00843-3>.
17. Spruijt, E. (2023). Open questions on liquid-liquid phase separation. *Commun. Chem.* *6*, 23. <https://doi.org/10.1038/s42004-023-00823-7>.
18. Naz, M., Zhang, L., Chen, C., Yang, S., Dou, H., Mann, S., and Li, J. (2024). Self-assembly of stabilized droplets from liquid-liquid phase separation for higher-order structures and functions. *Commun. Chem.* *7*, 79. <https://doi.org/10.1038/s42004-024-01168-5>.
19. Fisher, R.S., and Elbaum-Garfinkle, S. (2020). Tunable multiphase dynamics of arginine and lysine liquid condensates. *Nat. Commun.* *11*, 4628. <https://doi.org/10.1038/s41467-020-18224-y>.
20. Darling, A.L., and Shorter, J. (2021). Combating deleterious phase transitions in neurodegenerative disease. *Biochim. Biophys. Acta. Mol. Cell Res.* *1868*, 118984. <https://doi.org/10.1016/j.bbamcr.2021.118984>.
21. Hurtle, B.T., Xie, L., and Donnelly, C.J. (2023). Disrupting pathologic phase transitions in neurodegeneration. *J. Clin. Investig.* *133*, e168549. <https://doi.org/10.1172/JCI168549>.
22. Freibaum, B.D., Messing, J., Nakamura, H., Yurtsever, U., Wu, J., Kim, H.J., Hixon, J., Lemieux, R.M., Duffner, J., Huynh, W., et al. (2024). Identification of small molecule inhibitors of G3BP-driven stress granule formation. *J. Cell Biol.* *223*, e202308083. <https://doi.org/10.1083/jcb.202308083>.
23. Dignon, G.L., Zheng, W., and Mittal, J. (2019). Simulation methods for liquid-liquid phase separation of disordered proteins. *Curr. Opin. Chem. Eng.* *23*, 92–98. <https://doi.org/10.1016/j.coche.2019.03.004>.

24. Ruff, K.M., Dar, F., and Pappu, R.V. (2021). Polyphasic linkage and the impact of ligand binding on the regulation of biomolecular condensates. *Biophys. Rev. (Melville)* 2, 021302. <https://doi.org/10.1063/5.0050059>.
25. Mittag, T., and Pappu, R.V. (2022). A conceptual framework for understanding phase separation and addressing open questions and challenges. *Mol. Cell* 82, 2201–2214. <https://doi.org/10.1016/j.molcel.2022.05.018>.
26. Harmon, T.S., Holehouse, A.S., Rosen, M.K., and Pappu, R.V. (2017). Intrinsically disordered linkers determine the interplay between phase separation and gelation in multivalent proteins. *Elife* 6, e30294. <https://doi.org/10.7554/eLife.30294>.
27. GrandPre, T., Zhang, Y., Pyo, A.G.T., Weiner, B., Li, J.L., Jonikas, M.C., and Wingreen, N.S. (2023). Effects of linker length on phase separation: lessons from the Rubisco-EPYC1 system of the algal pyrenoid. Preprint at bioRxiv. <https://doi.org/10.1101/2023.06.11.544494>.
28. Howard, M.P., Jadrlich, R.B., Lindquist, B.A., Khabaz, F., Bonneceze, R.T., Milliron, D.J., and Truskett, T.M. (2019). Structure and phase behavior of polymer-linked colloidal gels. *J. Chem. Phys.* 151, 124901. <https://doi.org/10.1063/1.5119359>.
29. Sanchez-Burgos, I., Espinosa, J.R., Joseph, J.A., and Collepardo-Guevara, R. (2022). RNA length has a non-trivial effect in the stability of biomolecular condensates formed by RNA-binding proteins. *PLoS Comput. Biol.* 18, e1009810. <https://doi.org/10.1371/journal.pcbi.1009810>.
30. Ranganathan, S., and Shakhnovich, E.I. (2020). Dynamic metastable long-living droplets formed by sticker-spacer proteins. *Elife* 9, e56159. <https://doi.org/10.7554/eLife.56159>.
31. Brown, K., Chew, P.Y., Ingersoll, S., Espinosa, J.R., Aguirre, A., Espinoza, A., Wen, J., Astatike, K., Kutateladze, T.G., Collepardo-Guevara, R., and Ren, X. (2023). Principles of assembly and regulation of condensates of Polycomb repressive complex 1 through phase separation. *Cell Rep.* 42, 113136. <https://doi.org/10.1016/j.celrep.2023.113136>.
32. He, S., Chou, H.T., Matthies, D., Wunder, T., Meyer, M.T., Atkinson, N., Martinez-Sanchez, A., Jeffrey, P.D., Port, S.A., Patena, W., et al. (2020). The structural basis of Rubisco phase separation in the pyrenoid. *Nat. Plants* 6, 1480–1490. <https://doi.org/10.1038/s41477-020-00811-y>.
33. Kim, K., Saneyoshi, T., Hosokawa, T., Okamoto, K., and Hayashi, Y. (2016). Interplay of enzymatic and structural functions of CaMKII in long-term potentiation. *J. Neurochem.* 139, 959–972. <https://doi.org/10.1111/jnc.13672>.
34. Tullis, J.E., Larsen, M.E., Rumian, N.L., Freund, R.K., Boxer, E.E., Brown, C.N., Coultrap, S.J., Schulman, H., Aoto, J., Dell'Acqua, M.L., and Bayer, K.U. (2023). LTP induction by structural rather than enzymatic functions of CaMKII. *Nature* 621, 146–153. <https://doi.org/10.1038/s41586-023-06465-y>.
35. Yasuda, R., Hayashi, Y., and Hell, J.W. (2022). CaMKII: a central molecular organizer of synaptic plasticity, learning and memory. *Nat. Rev. Neurosci.* 23, 666–682. <https://doi.org/10.1038/s41583-022-00624-2>.
36. Zeng, M., Diaz-Alonso, J., Ye, F., Chen, X., Xu, J., Ji, Z., Nicoll, R.A., and Zhang, M. (2019). Phase separation-mediated TARP/MAGUK complex condensation and AMPA receptor synaptic transmission. *Neuron* 104, 529–543.e6. <https://doi.org/10.1016/j.neuron.2019.08.001>.
37. Gouveia, B., Kim, Y., Shaevitz, J.W., Petry, S., Stone, H.A., and Brangwynne, C.P. (2022). Capillary forces generated by biomolecular condensates. *Nature* 609, 255–264. <https://doi.org/10.1038/s41586-022-05138-6>.
38. Choi, J.M., Dar, F., and Pappu, R.V. (2019). LASSI: A lattice model for simulating phase transitions of multivalent proteins. *PLoS Comput. Biol.* 15, e1007028. <https://doi.org/10.1371/journal.pcbi.1007028>.
39. Farag, M., Borchers, W.M., Bremer, A., Mittag, T., and Pappu, R.V. (2023). Phase separation of protein mixtures is driven by the interplay of homotypic and heterotypic interactions. *Nat. Commun.* 14, 5527. <https://doi.org/10.1038/s41467-023-41274-x>.
40. Farag, M., Cohen, S.R., Borchers, W.M., Bremer, A., Mittag, T., and Pappu, R.V. (2022). Condensates formed by prion-like low-complexity domains have small-world network structures and interfaces defined by expanded conformations. *Nat. Commun.* 13, 7722. <https://doi.org/10.1038/s41467-022-35370-7>.
41. King, M.R., Ruff, K.M., Lin, A.Z., Pant, A., Farag, M., Lalmansingh, J.M., Wu, T., Fossat, M.J., Ouyang, W., Lew, M.D., et al. (2024). Macromolecular condensation organizes nucleolar sub-phases to set up a pH gradient. *Cell* 187, 1889–1906.e24. <https://doi.org/10.1016/j.cell.2024.02.029>.
42. Vistrup-Parry, M., Chen, X., Johansen, T.L., Bach, S., Buch-Larsen, S.C., Bartling, C.R.O., Ma, C., Clemmensen, L.S., Nielsen, M.L., Zhang, M., and Strømgaard, K. (2021). Site-specific phosphorylation of PSD-95 dynamically regulates the postsynaptic density as observed by phase separation. *iScience* 24, 103268. <https://doi.org/10.1016/j.isci.2021.103268>.
43. Ravi, A.S., Zeng, M., Chen, X., Sandoval, G., Diaz-Alonso, J., Zhang, M., and Nicoll, R.A. (2022). Long-term potentiation reconstituted with an artificial TARP/PSD-95 complex. *Cell Rep.* 41, 111483. <https://doi.org/10.1016/j.celrep.2022.111483>.
44. Zeng, M., Chen, X., Guan, D., Xu, J., Wu, H., Tong, P., and Zhang, M. (2018). Reconstituted postsynaptic density as a molecular platform for understanding synapse formation and plasticity. *Cell* 174, 1172–1187.e16. <https://doi.org/10.1016/j.cell.2018.06.047>.
45. Rosenberg, O.S., Deindl, S., Sung, R.J., Nairn, A.C., and Kuriyan, J. (2005). Structure of the autoinhibited kinase domain of CaMKII and SAXS analysis of the holoenzyme. *Cell* 123, 849–860. <https://doi.org/10.1016/j.cell.2005.10.029>.
46. Bayer, K.U., De Koninck, P., Leonard, A.S., Hell, J.W., and Schulman, H. (2001). Interaction with the NMDA receptor locks CaMKII in an active conformation. *Nature* 411, 801–805. <https://doi.org/10.1038/35081080>.
47. Yamada, R., and Takada, S. (2023). Postsynaptic protein assembly in three and two dimensions studied by mesoscopic simulations. *Biophys. J.* 122, 3395–3410. <https://doi.org/10.1016/j.bpj.2023.07.015>.
48. Cai, Q., Chen, X., Zhu, S., Nicoll, R.A., and Zhang, M. (2023). Differential roles of CaMKII isoforms in phase separation with NMDA receptors and in synaptic plasticity. *Cell Rep.* 42, 112146. <https://doi.org/10.1016/j.celrep.2023.112146>.
49. Li, P., Banjade, S., Cheng, H.C., Kim, S., Chen, B., Guo, L., Llaguno, M., Hollingsworth, J.V., King, D.S., Banani, S.F., et al. (2012). Phase transitions in the assembly of multivalent signalling proteins. *Nature* 483, 336–340. <https://doi.org/10.1038/nature10879>.
50. Espinosa, J.R., Joseph, J.A., Sanchez-Burgos, I., Garaizar, A., Frenkel, D., and Collepardo-Guevara, R. (2020). Liquid network connectivity regulates the stability and composition of biomolecular condensates with many components. *Proc. Natl. Acad. Sci. USA* 117, 13238–13247. <https://doi.org/10.1073/pnas.1917569117>.
51. Israelachvili, J.N. (2011). *Intermolecular and Surface Forces*, 3rd Edition (Academic Press). <https://doi.org/10.1016/C2009-0-21560-1>.
52. Guzowski, J., Korczyk, P.M., Jakiela, S., and Garstecki, P. (2012). The structure and stability of multiple micro-droplets. *Soft Matter* 8, 7269–7278. <https://doi.org/10.1039/C2SM25838B>.
53. Watts, D.J., and Strogatz, S.H. (1998). Collective dynamics of 'small-world' networks. *Nature* 393, 440–442. <https://doi.org/10.1038/30918>.
54. Nawrocki, G., Wang, P.H., Yu, I., Sugita, Y., and Feig, M. (2017). Slow-down in diffusion in crowded protein solutions correlates with transient cluster formation. *J. Phys. Chem. B* 121, 11072–11084. <https://doi.org/10.1021/acs.jpcc.7b08785>.
55. von Bulow, S., Siggel, M., Linke, M., and Hummer, G. (2019). Dynamic cluster formation determines viscosity and diffusion in dense protein solutions. *Proc. Natl. Acad. Sci. USA* 116, 9843–9852. <https://doi.org/10.1073/pnas.1817564116>.
56. Lee, D.S.W., Wingreen, N.S., and Brangwynne, C.P. (2021). Chromatin mechanics dictates subdiffusion and coarsening dynamics of embedded

- condensates. *Nat. Phys.* 17, 531–538. <https://doi.org/10.1038/s41567-020-01125-8>.
57. Su, W.C., Ho, J.C.S., Gettel, D.L., Rowland, A.T., Keating, C.D., and Parikh, A.N. (2024). Kinetic control of shape deformations and membrane phase separation inside giant vesicles. *Nat. Chem.* 16, 54–62. <https://doi.org/10.1038/s41557-023-01267-1>.
58. Lifshitz, I.M., and Slyozov, V.V. (1961). The kinetics of precipitation from supersaturated solid solutions. *J. Phys. Chem. Solids* 19, 35–50. [https://doi.org/10.1016/0022-3697\(61\)90054-3](https://doi.org/10.1016/0022-3697(61)90054-3).
59. Okamoto, K., Bosch, M., and Hayashi, Y. (2009). The roles of CaMKII and F-actin in the structural plasticity of dendritic spines: a potential molecular identity of a synaptic tag? *Physiology* 24, 357–366. <https://doi.org/10.1152/physiol.00029.2009>.
60. Nakashima, K.K., van Haren, M.H.I., André, A.A.M., Robu, I., and Spruijt, E. (2021). Active coacervate droplets are protocells that grow and resist Ostwald ripening. *Nat. Commun.* 12, 3819. <https://doi.org/10.1038/s41467-021-24111-x>.
61. Keber, F.C., Nguyen, T., Mariossi, A., Brangwynne, C.P., and Wühr, M. (2024). Evidence for widespread cytoplasmic structuring into mesoscale condensates. *Nat. Cell Biol.* 26, 346–352. <https://doi.org/10.1038/s41556-024-01363-5>.
62. Cai, Q., Zeng, M., Wu, X., Wu, H., Zhan, Y., Tian, R., and Zhang, M. (2021). CaMKII $\alpha$ -driven, phosphatase-checked postsynaptic plasticity via phase separation. *Cell Res.* 31, 37–51. <https://doi.org/10.1038/s41422-020-00439-9>.
63. Fleming, I.N., Elliott, C.M., Buchanan, F.G., Downes, C.P., and Exton, J.H. (1999). Ca<sup>2+</sup>/calmodulin-dependent protein kinase II regulates Tiam1 by reversible protein phosphorylation. *J. Biol. Chem.* 274, 12753–12758. <https://doi.org/10.1074/jbc.274.18.12753>.
64. Saneyoshi, T., Matsuno, H., Suzuki, A., Murakoshi, H., Hedrick, N.G., Agnello, E., O'Connell, R., Stratton, M.M., Yasuda, R., and Hayashi, Y. (2019). Reciprocal activation within a kinase-effector complex underlying persistence of structural LTP. *Neuron* 102, 1199–1210.e6. <https://doi.org/10.1016/j.neuron.2019.04.012>.
65. Hudmon, A., Kim, S.A., Kolb, S.J., Stoops, J.K., and Waxham, M.N. (2001). Light scattering and transmission electron microscopy studies reveal a mechanism for calcium/calmodulin-dependent protein kinase II self-association. *J. Neurochem.* 76, 1364–1375. <https://doi.org/10.1046/j.1471-4159.2001.00119.x>.
66. Hudmon, A., Lebel, E., Roy, H., Sik, A., Schulman, H., Waxham, M.N., and De Koninck, P. (2005). A mechanism for Ca<sup>2+</sup>/calmodulin-dependent protein kinase II clustering at synaptic and nonsynaptic sites based on self-association. *J. Neurosci.* 25, 6971–6983. <https://doi.org/10.1523/JNEUROSCI.4698-04.2005>.
67. Tsujioka, S., Sumino, A., Nagasawa, Y., Sumikama, T., Flechsig, H., Puppulin, L., Tomita, T., Baba, Y., Kakuta, T., Ogoshi, T., et al. (2023). Imaging single CaMKII holoenzymes at work by high-speed atomic force microscopy. *Sci. Adv.* 9, eadh1069. <https://doi.org/10.1126/sciadv.adh1069>.
68. Naisbitt, S., Kim, E., Tu, J.C., Xiao, B., Sala, C., Valtschanoff, J., Weinberg, R.J., Worley, P.F., and Sheng, M. (1999). Shank, a novel family of postsynaptic density proteins that binds to the NMDA receptor/PSD-95/GKAP complex and cortactin. *Neuron* 23, 569–582. [https://doi.org/10.1016/s0896-6273\(00\)80809-0](https://doi.org/10.1016/s0896-6273(00)80809-0).
69. Kim, J.H., Liao, D., Lau, L.F., and Huganir, R.L. (1998). SynGAP: a synaptic RasGAP that associates with the PSD-95/SAP90 protein family. *Neuron* 20, 683–691. [https://doi.org/10.1016/s0896-6273\(00\)81008-9](https://doi.org/10.1016/s0896-6273(00)81008-9).
70. Irie, M., Hata, Y., Takeuchi, M., Ichtchenko, K., Toyoda, A., Hirao, K., Takai, Y., Rosahl, T.W., and Südhof, T.C. (1997). Binding of neuroligins to PSD-95. *Science* 277, 1511–1515. <https://doi.org/10.1126/science.277.5331.1511>.
71. Kim, N., Yun, H., Lee, H., and Yoo, J.Y. (2024). Interplay between membranes and biomolecular condensates in the regulation of membrane-associated cellular processes. *Exp. Mol. Med.* 56, 2357–2364. <https://doi.org/10.1038/s12276-024-01337-5>.
72. Hagberg, A.A., Schult, D.A., and Swart, P.J. (2008). Exploring network structure, dynamics, and function using NetworkX. In the 7th Python in Science Conference (SciPy2008) Held in Pasadena, CA USA, pp. 11–15.
73. Stukowski, A. (2010). Visualization and analysis of atomistic simulation data with OVITO—the Open Visualization Tool. *Modelling Simul. Mater. Sci. Eng.* 18, 015012. <https://doi.org/10.1088/0965-0393/18/1/015012>.
74. Dawson-Haggerty, M. (2022). Trimesh 3.12.7. <https://trimesh.org/>.
75. Sullivan, C., and Kaszynski, A. (2019). PyVista: 3D plotting and mesh analysis through a streamlined interface for the Visualization Toolkit (VTK). *J. Open Source Softw.* 4, 1450. <https://doi.org/10.21105/joss.01450>.
76. Van der Walt, S., Schönberger, J.L., Nunez-Iglesias, J., Boulogne, F., Warner, J.D., Yager, N., Gouillart, E., and Yu, T.; scikit-image contributors (2014). Scikit-image: image processing in Python. *PeerJ* 2, e453. <https://doi.org/10.7717/peerj.453>.
77. Wall, M.A., Socolich, M., and Ranganathan, R. (2000). The structural basis for red fluorescence in the tetrameric GFP homolog DsRed. *Nat. Struct. Biol.* 7, 1133–1138. <https://doi.org/10.1038/81992>.
78. Kim, K.S., Yan, D., and Tomita, S. (2010). Assembly and stoichiometry of the AMPA receptor and transmembrane AMPA receptor regulatory protein complex. *J. Neurosci.* 30, 1064–1072. <https://doi.org/10.1523/JNEUROSCI.3909-09.2010>.
79. Shcherbo, D., Shemiakina, I.I., Ryabova, A.V., Luker, K.E., Schmidt, B.T., Souslova, E.A., Gorodnicheva, T.V., Strukova, L., Shidlovskiy, K.M., Britanova, O.V., et al. (2010). Near-infrared fluorescent proteins. *Nat. Methods* 7, 827–829. <https://doi.org/10.1038/nmeth.1501>.
80. Traynelis, S.F., Wollmuth, L.P., McBain, C.J., Menniti, F.S., Vance, K.M., Ogden, K.K., Hansen, K.B., Yuan, H., Myers, S.J., and Dingledine, R. (2010). Glutamate receptor ion channels: structure, regulation, and function. *Pharmacol. Rev.* 62, 405–496. <https://doi.org/10.1124/pr.109.002451>.
81. Myers, J.B., Zaegel, V., Coultrap, S.J., Miller, A.P., Bayer, K.U., and Reichow, S.L. (2017). The CaMKII holoenzyme structure in activation-competent conformations. *Nat. Commun.* 8, 15742. <https://doi.org/10.1038/ncomms15742>.
82. Shaikh, S.A., Dolino, D.M., Lee, G., Chatterjee, S., MacLean, D.M., Flatebo, C., Landes, C.F., and Jayaraman, V. (2016). Stargazin Modulation of AMPA Receptors. *Cell Rep.* 17, 328–335. <https://doi.org/10.1016/j.celrep.2016.09.014>.
83. Tian, M., Stroebel, D., Piot, L., David, M., Ye, S., and Paoletti, P. (2021). GluN2A and GluN2B NMDA receptors use distinct allosteric routes. *Nat. Commun.* 12, 4709. <https://doi.org/10.1038/s41467-021-25058-9>.
84. Pletnev, S., Subach, F.V., Dauter, Z., Wlodawer, A., and Verkhusa, V.V. (2012). A structural basis for reversible photoswitching of absorbance spectra in red fluorescent protein rsTagRFP. *J. Mol. Biol.* 417, 144–151. <https://doi.org/10.1016/j.jmb.2012.01.044>.
85. Urakubo, H., Sato, M., Ishii, S., and Kuroda, S. (2014). *In vitro* reconstitution of a CaMKII memory switch by an NMDA receptor-derived peptide. *Biophys. J.* 106, 1414–1420. <https://doi.org/10.1016/j.bpj.2014.01.026>.
86. Özden, C., Sloutsky, R., Mitsugi, T., Santos, N., Agnello, E., Gaubitz, C., Foster, J., Lapinskas, E., Esposito, E.A., Saneyoshi, T., et al. (2022). CaMKII binds both substrates and activators at the active site. *Cell Rep.* 40, 111064. <https://doi.org/10.1016/j.celrep.2022.111064>.
87. Christensen, N.R., Pedersen, C.P., Sereikaite, V., Pedersen, J.N., Vistrup-Parry, M., Sørensen, A.T., Otzen, D., Teilum, K., Madsen, K.L., and Strømgaard, K. (2022). Bidirectional protein-protein interactions control liquid-liquid phase separation of PSD-95 and its interaction partners. *iScience* 25, 103808. <https://doi.org/10.1016/j.isci.2022.103808>.
88. Girvan, M., and Newman, M.E.J. (2002). Community structure in social and biological networks. *Proc. Natl. Acad. Sci. USA* 99, 7821–7826. <https://doi.org/10.1073/pnas.122653799>.

## Q5 Q6 STAR★METHODS

### KEY RESOURCES TABLE

REAGENT or RESOURCE	SOURCE	IDENTIFIER
<b>Bacterial and virus strains</b>		
<i>Escherichia coli</i> : BL21 DE3 RIL	Agilent	Cat# 230245
<b>Chemicals, peptides, and recombinant proteins</b>		
Recombinant protein: CaMKII	Hosokawa et al. <sup>16</sup>	N/A
Recombinant protein: eqFP670-tagged GluN2Bc	Hosokawa et al. <sup>16</sup>	N/A
Recombinant protein: PSD-95	Zeng et al. <sup>44</sup>	N/A
Recombinant protein: dsRed2-tagged STGc	Hosokawa et al. <sup>16</sup>	N/A
Recombinant protein: CaM	Zeng et al. <sup>44</sup>	N/A
Chemical: iFlur405 NHS ester	AAT Bioquest	Cat# 1021
Chemical: iFlur488 NHS ester	AAT Bioquest	Cat# 1023
<b>Recombinant DNA</b>		
p32m3c-CaM	Zeng et al. <sup>44</sup>	N/A
p32m3c-PSD-95	Zeng et al. <sup>44</sup>	N/A
pSUMO-CaMKII $\zeta$	Hosokawa et al. <sup>16</sup>	N/A
pSUMO-Spy-tag-STGc	Zeng et al. <sup>44</sup>	N/A
pSUMO-Spy-tag-GluN2Bc	Hosokawa et al. <sup>16</sup>	N/A
pSUMO-DsRed2-Spy-catcher	Hosokawa et al. <sup>16</sup>	N/A
pSUMO-eqFP670-Spy-catcher	Hosokawa et al. <sup>16</sup>	N/A
<b>Software and algorithms</b>		
Code used for modeling and simulation	This manuscript, GitHub	<a href="https://github.com/pandeyv1990/modeling_and_simulation_PIPS_camkii">https://github.com/pandeyv1990/modeling_and_simulation_PIPS_camkii</a> ( <a href="https://doi.org/10.5281/zenodo.14957640">https://doi.org/10.5281/zenodo.14957640</a> )
Code used for analyses and visualization	This manuscript, GitHub	<a href="https://github.com/urakubo/analyses_PIPS_camkii">https://github.com/urakubo/analyses_PIPS_camkii</a> ( <a href="https://doi.org/10.5281/zenodo.14961116">https://doi.org/10.5281/zenodo.14961116</a> )
LaSSI	Choi et al., <sup>38</sup> GitHub	<a href="https://github.com/pappulab/LASSI">https://github.com/pappulab/LASSI</a>
NetworkX 3.1	Hagberg et al. <sup>72</sup>	<a href="https://networkx.org/">https://networkx.org/</a>
OVITO 3.10.2	Stukowski <sup>73</sup>	<a href="https://ovito.org/">https://ovito.org/</a>
Trimesh	Dawson-Haggerty <sup>74</sup>	<a href="https://trimesh.org/">https://trimesh.org/</a>
PyVista	Sullivan et al. <sup>75</sup>	<a href="https://pyvista.org/">https://pyvista.org/</a>
Scikit-image	Van der Walt et al. <sup>76</sup>	<a href="https://scikit-image.org/">https://scikit-image.org/</a>
Python 3.8.10	Python Software Foundation	<a href="https://python.org/">https://python.org/</a>
ImageJ	NIH	<a href="https://imagej.nih.gov/ij/">https://imagej.nih.gov/ij/</a>
<b>Other</b>		
Nickel-NTA	Nacalai Tesque	Cat# 6BCL-NTANI
Hiload 26/600 Suprdex 200 pg	GE Healthcare	Cat# 28989336
HiTrap Q HP	GE Healthcare	Cat# 17115401
Confocal Microscopy System	Olympus	FLUOVIEW FV1200

### EXPERIMENTAL MODEL AND STUDY PARTICIPANT DETAILS

#### Bacterial strain

*Escherichia coli* BL21-CodonPlus (DE3)-RIL cells (Agilent) were used in this study for the production of recombinant proteins. Cells were cultured in LB medium supplemented with necessary antibiotics.

## METHOD DETAILS

### *In vitro* phase separation experiment

Details of protein preparation are described elsewhere.<sup>16</sup> Briefly, PSD-95 with a thioredoxin tag and 3c protease site, CaMKII $\alpha$ , dsRed2-spy catcher, spy-tag-carboxyl tail of STG (STGc), eqFP670-spy catcher, and spy-tag-carboxyl tail of GluN2B (GluN2Bc) were expressed in *Escherichia coli* strain BL21 DE3 RIL. These proteins were first purified via affinity chromatography using a Ni-NTA column (Nacalai Tesque). Tags were removed by cleavage with corresponding protease, and the purified DsRed-spy catcher or eqFP670-spy catcher were combined with spy-tag-STGc or spy-tag-GluN2Bc, respectively, to enable protein ligation. Combined proteins were further purified via size exclusion chromatography using a Hiload 16/60 Superdex 200 with ÄKTA GO FPLC system (Cytiva). CaMKII was further purified by the HiTrap Q column (Cytiva). CaMKII and PSD-95 were stained with iFluor488 and iFluor405, respectively, by using succinimidyl ester (AAT bioquest).<sup>44</sup> The final purity of the proteins was visualized using Coomassie brilliant blue dye staining after SDS-polyacrylamide gel electrophoresis as shown in Figures 1A and 2A of Hosokawa et al.<sup>16</sup> Note that in the experimental solution described below, dsRed2 with STGc autonomously formed a tetramer.<sup>77</sup> This mimicked the AMPA-receptor complex incorporating four STGs,<sup>78</sup> as modeled in Figure 1B (bottom right). Similarly, eqFP670 with GluN2Bc formed a dimer,<sup>79</sup> mimicking an NMDA-receptor complex incorporating two GluN2Bs.<sup>80</sup> This was modeled in Figure 1B (top right).

Purified proteins were combined in the observation buffer 50 mM Tris-HCl pH 8.0, 100 mM NaCl, and 1 mM TCEP in the presence of 20  $\mu$ M calmodulin, 1 mM MgCl<sub>2</sub>, 1 mM ATP, and 1 mM CaCl<sub>2</sub> to activate CaMKII. The final mixtures contained iFluor488-tagged CaMKII (CaMKII), eqFP670-tagged GluN2Bc (GluN2B), iFluor405-tagged PSD-95 (PSD-95), and dsRed2-tagged STGc (STG) at indicated concentrations. Protein concentration is denoted as monomer concentration throughout the study.

For observation, a sample chamber was made between a coverslip (12 mm round coverslip, MATSUNAMI) and a slide glass (FRC-04, MATSUNAMI) separated by double-sided adhesive paper tape. The protein mixture (5  $\mu$ L) was injected into this space and the condensates were allowed to settle to the bottom of the coverslip for 5 min. Although they were untreated bare glasses, the absorption of the condensates was minimal, and nonspecific binding to the glasses was not observed at the level of fluorescence imaging.<sup>16</sup> Condensates were observed using a confocal microscopy (FLUOVIEW FV1200, Olympus; 100 $\times$  Oil immersion objective lens; photomultiplier tube detection). The images for each color channel were obtained using an LD/MultiAr laser and the excitation wavelengths were as follows: 488 nm for iFluor-488-tagged CaMKII, 405 nm for iFluor-405-tagged PSD-95, 546 nm for dsRed2-tagged STGc, and 647 nm for eqFP670-tagged GluN2Bc.

### LaSSI simulation

Simulations were performed on the LaSSI-simulation engine, which was developed for the MC simulation at coarse-graining levels.<sup>38</sup> All simulations were conducted in a 120  $\times$  120  $\times$  120 cubic lattice with periodic boundary conditions. The  $\sqrt{3}$  unit length of the cubic lattice was set as the unit length “lattice site” (l.s.) because this is used as the unit length of interactions and connections.<sup>38</sup> Various MC moves were implemented in LaSSI. The types and frequencies of MC moves used in the present study are described in Table S1. Protein concentrations are described in Table S2.

### Linker length

The maximal linker lengths between the beads of CaMKII, GluN2B, PSD-95, and STG were set to 3, 2, 2, and 2 l.s., respectively. These lengths were determined based on the relative sizes of the protein domains as follows: CaMKII (70–140 Å),<sup>81</sup> STG and its mimic (dsRed2-tagged STGc) (30–50 Å),<sup>77,82</sup> PSD-95 ( $\sim$ 40 Å), and GluN2B and its mimic (eqFP670-tagged GluN2Bc) ( $\sim$ 50 Å).<sup>79,83,84</sup> They were not mapped to absolute lengths as in other schematic models.<sup>7,9,10,38,41</sup>

### Binding energy

Site-specific interactions were determined based on published binding affinities. We adopted  $-3.5$ ,  $-5.25$ , and  $-3.0 k_B T$  as binding energies between CaMKII and GluN2B,<sup>85,86</sup> GluN2B and PSD-95,<sup>42,44</sup> and PSD-95 and STG,<sup>42,87</sup> respectively (Figure 1C). Note, these shared similar energies because they had similar binding affinities.

IDR-mediated interactions were also determined based on the literature. In particular, the carboxyl tail of STG is rich in arginine residues, and a study reports that these produce a strong IDR-mediated affinity with PSD-95.<sup>44</sup> The carboxyl tail of GluN2B also contains arginine residues. We thus assigned values of  $-0.1$ ,  $-0.11$ ,  $-0.10$ , and  $-0.12 k_B T$  as the affinities between STG and STG, STG and PSD-95, STG and CaMKII, and STG and GluN2B, respectively (Figure 1D). Furthermore, all four proteins have electrically charged residues in their IDRs, which may cause IDR-mediated interactions. Thus, a small uniform affinity ( $-0.05 k_B T$ ) was assigned between all the beads as a baseline (Figure 1D). The baseline affinity accounted for hydrophobicity and the other minor forces including the  $\pi$ - $\pi$ , cation-anion, dipole-dipole, and  $\pi$ -cation interactions.<sup>9,10</sup>

### Simulation time schedule

Each simulation began with random initial conditions, a system temperature of  $1000 T^*$ , and the following spherical constraining potential:

$$\frac{V(r)}{T^*} = \begin{cases} r & (r \geq R_c) \\ 0 & (r < R_c) \end{cases} \quad (\text{Equation 1})$$

Where  $r$  denotes the distance from the center of the lattice space,  $R_c = \sqrt[3]{N_{\text{beads}}/\pi}$ ,  $N_{\text{beads}}$  denotes the total number of beads, and  $T^*$  denotes the unit of normalized temperature ( $k_B T/\epsilon$ ).<sup>38</sup> This constraining potential was introduced following preceding studies<sup>9,12</sup> to push all beads toward the center of the lattice space. The simulation ran over  $5.0 \times 10^7$  MC steps, then the system temperature was discontinuously decreased to  $3.2 T^*$  (Step 1, Table S3). The simulation further ran over  $1.0 \times 10^8$  MC steps while decreasing the system temperature linearly from  $3.2$  to  $1.0 T^*$  or from  $3.2$  to  $1.2 T^*$  (Step 2, Table S3). Then, the constraining potential was turned off, and the simulation ran over  $1.0 \times 10^{11}$  steps. The temperature was kept at  $1.0$  or  $1.2 T^*$  (Step 3, Table S3). This time schedule enabled rapid convergence to the steady states.

Simulation results at the final time frame were collected for analysis. The last five time frames with an interval of  $2 \times 10^9$  MC steps were averaged to generate RDPs.

For Video S1, we first mixed inactive CaMKII, GluN2B, STG, and PSD-95, in which the inactive CaMKII was designed to not bind to any other proteins. The simulation ran standardized steps 1, 2, and 3 to reach an equilibrium state (Table S3). After these steps, we observed an STG–PSD-95–GluN2B condensate and CaMKII in the diluted phase (Figures S1G–S1I). CaMKII was then activated and the simulation continued until the next equilibrium state (steps 4 and 5 in Table S3). During step 4, the system temperature was linearly increased from  $1.0 T^*$  to  $1.2 T^*$  for rapid convergence. Video S1 shows the transition of the condensate during steps 4 and 5.

## QUANTIFICATION AND STATISTICAL ANALYSIS

### Visualization

Steady-state profiles of mixtures were visualized using the following four methods. First, protein bead distributions in the 3D space were visualized using OVITO 3.10.2.<sup>73</sup> Front halves were removed, and only the rear halves are shown in Figures 1, S1, and S10 for their visibility.

Second, protein beads were blurred by the Gaussian kernel with a standard deviation (SD) of 1.15 l.s., and their intensity levels are shown at the section that divided the center of the condensate (Figures 1F, 1I, 1L, 2A–2C, 3H, 4A–4D, S1B, S1E S1H, S1M, and S5D). Intensity levels were normalized by the maximal level.

Third, RDPs from the condensate center-of-mass were generated according to previous literature.<sup>12,38</sup> Briefly, the number histograms of each protein bead binning a unit sphere,  $H(\gamma_n)$ , were first calculated, then divided by the number histograms of lattice sites,  $H_o(\gamma_n)$  as follows:

$$\rho(\gamma_n) = \frac{H(\gamma_n)}{H_o(\gamma_n)} \quad (\text{Equation 2})$$

Where  $\gamma_n$  denotes bins with a shell thickness of  $1/\sqrt{3}$  l.s., and  $\rho(\gamma_n)$  gives the volume-occupation ratios of target proteins. The means and SDs were plotted based on data at five sampling time points with an interval of  $2 \times 10^9$  MC steps (Figures 1G, 1J, 1M, 2A–2C, 3H, 4A–4D, 6A, 6B, S1C, S1F, S1I, S1N, and S5D). This averaging was effective in compensating small sampling volumes in the small radius bins.

Fourth, the 3D shapes of the condensates were visualized using their rendered volumes (Figures 2A–2C, 4E, 5, S2, and S7A). Except for the volumes in Figures 2A–2C, and S7A, all proteins were first rotated so that the barycenter of CaMKII beads was located on the left and that of PSD-95 beads was on the right. Then, the half maximal levels of blurred CaMKII and STG (Gaussian filter,  $\sigma = 1.15$  l.s.) were used for the isosurface values for the marching cubes algorithm (Scikit-image 0.21.0),<sup>76</sup> and obtained surface meshes were smoothed using the Humpy filter ( $\alpha = 1.0$  and  $\beta = 0.0$ , Trimesh 3.12.7).<sup>74</sup> Smoothed meshes were visualized using Pyvista 0.43.3<sup>75</sup> and used to determine the phase diagram of the condensates together with their sectioned intensity levels (Figures 2H, 4F and S2).

### Surface tension

The MC sampling of LaSSI was intended to obtain the steady-state spatial distribution of beads, and linkers of LaSSI lack the tension associated with macroscopic characteristics of condensates. Nevertheless, a fully stretched linker prevents the tethered beads from being further apart, and in more realistic situations, this spatial constraint should produce tension. The summed tension directed to the center of condensate corresponds to the cohesion force, whereas the tangential forces are neutralized under the spherical symmetry. If the cohesion force is divided by  $2\pi r$ , where  $r$  is the radius of the condensate, this forms a surface tension under the spherical symmetry condition.<sup>51</sup>

$$\text{Surface tension} \propto \frac{1}{2\pi R_{\text{condensate}}} \sum_i f(r_i) \cos(\theta_i) \quad (\text{Equation 3})$$

Where  $r_i$  is the distance of  $i$ th CaMKII-binding bead from the hub bead, and  $f(r)$  is the relative strength of putative surface tension, which should have a positive value for almost fully stretched linkers. As an analogy to the local MC move of bead  $i$  being selected from the uniform distribution  $[-2, 2]$  and the MC move being rejected if  $r_i$  exceeded the linker length,<sup>38</sup>  $f(r)$  was assumed as:

$$f(r) = \begin{cases} (r - L_{\text{linker}} + 2)/2 & (r \geq L_{\text{linker}} - 2) \\ 0 & (r < L_{\text{linker}} - 2) \end{cases} \quad (\text{Equation 4})$$

Where  $L_{\text{linker}}$  denotes the linker length.

### Surface tension and topology of a two-phase condensate

Topology of a two-phase condensate is connected with surface tension as follows.<sup>7,11,37,52</sup> Suppose that two immiscible liquids A and B form a partial engulfment structure with the contact angles  $\theta_A$  and  $\theta_B$ , respectively. In this situation, the balance of forces acting on the two-phase contact line can be described using the Neumann's triangle.<sup>52</sup>

$$\begin{aligned} \gamma_{AB} \cos \theta_B + \gamma_B + \gamma_A \cos(\theta_A + \theta_B) &= 0 \\ \gamma_{AB} \cos \theta_A + \gamma_A + \gamma_B \cos(\theta_A + \theta_B) &= 0 \end{aligned} \quad (\text{Equation 5})$$

where  $\gamma_A$  and  $\gamma_B$  are the surface tensions of A and B, respectively, and  $\gamma_{AB}$  is the interfacial tension. Partial engulfment needs to satisfy Equation 5, which can be rewritten as:

$$\cos \theta_A = \frac{\gamma_B^2 - \gamma_A^2 - \gamma_{AB}^2}{2\gamma_A\gamma_{AB}} \quad (\text{Equation 6})$$

For the above equation to hold and  $\pi > \theta_A > 0$ ,

$$\begin{aligned} 1 &> \frac{\gamma_B^2 - \gamma_A^2 - \gamma_{AB}^2}{2\gamma_A\gamma_{AB}} \\ \frac{\gamma_B^2 - \gamma_A^2 - \gamma_{AB}^2}{2\gamma_A\gamma_{AB}} &> -1 \end{aligned} \quad (\text{Equation 7})$$

The first line of Equation 7 can be rewritten under  $\gamma_A > 0$ ,  $\gamma_B > 0$ , and  $\gamma_{AB} > 0$ :

$$\gamma_B < \gamma_A + \gamma_{AB} \quad (\text{Equation 8})$$

Equation 8 is the requirement for liquid B to not be fully wrapped by liquid A. Replacing A and B with STG and CaMKII, respectively, results in the inequalities in Figure 5J ( $\gamma_{\text{STG}} < \gamma_{\text{CaMKII}} + \gamma_{\text{CaMKII,STG}}$ ). Note that the second line of Equation 7 results in  $\gamma_A < \gamma_B + \gamma_{AB}$ . This denotes the requirement for liquid A to not be fully wrapped by liquid B. Also, to hold  $\pi > \theta_A > 0$  and  $\pi > \theta_B > 0$ ,  $\gamma_A + \gamma_B > \gamma_{AB}$  is required. This is required for the attachment of liquids A and B together. Details of the derivation, including further characterization of partial engulfment, are described in Guzowski et al.<sup>52</sup>

### Connectivity analyses

The connections through site-specific interactions were examined using NetworkX 3.1.<sup>72</sup> Each LAMMPS file from LaSSI was converted to an undirected multigraph, and the number of connected proteins were counted (Figures 3A, 3C, and 3F).

### Graph theoretical analyses

We identified the CaMKII–GluN2B condensate as the largest connected network, (Figures 5 and 6).<sup>40</sup> The connected network was further simplified into the graph that represented the connectivity of CaMKII proteins through GluN2B. In the CaMKII network, the CC for  $i$ th CaMKII protein,  $CC_i$ , was calculated based on the following equation:<sup>39,53</sup>

$$CC_i = \frac{2}{k_i(k_i - 1)} |\{e_{jk} : v_j, v_k \in N_i, e_{jk} \in E\}| \quad (\text{Equation 9})$$

Where  $N_i$  denotes the set of CaMKII bound to the  $i$ th CaMKII,  $E$  denotes the set of binding edges,  $k_i$  denotes the number of the bound CaMKII, and  $e_{jk}$  denotes the binding edge between  $j$ th CaMKII,  $v_j$ , and  $k$ th CaMKII,  $v_k$ . This corresponds to Figure 7D, and intuitively,  $CC_i$  denotes the number ratio of the formation of the triangular connection between CaMKII, one of which is the  $i$ th CaMKII. Then, the averaged CC,  $\overline{CC}$ , is defined as:

$$\overline{CC} = \frac{1}{n_{\text{CaMKII}}} \sum_{i=1}^{n_{\text{CaMKII}}} CC_i \quad (\text{Equation 10})$$

Where  $n_{\text{CaMKII}}$  denotes the number of CaMKII in the CaMKII network. The CC has a value in the range of  $[0, 1]$ , and the higher value indicates a denser connectivity. We compared the averaged CC with the recovery rate from the photobleaching (Figures 7C, 7E, and 7F).

The overall characteristics of the CaMKII network were quantified using the Girvan–Newman algorithm for community detection (Figures 7G and 7H) as described previously.<sup>88</sup> Here, the Girvan–Newman algorithm targets the CaMKII network and progressively removes edges (CaMKII–CaMKII connections) from this network. The removal was performed on the edge that showed the highest edge-betweenness centrality, i.e., the most important edge to form the connected condensate. The repeats of the removal split the CaMKII network into multiple connected networks. This process was depicted as a dendrogram (Figures 7G and 7H).

To evaluate the global characteristics of the CaMKII network, we used the modularity,  $Q$ , as a measure of modular structure:

$$Q = \frac{1}{2m} \sum_{ij} \left[ A_{ij} - \frac{k_i k_j}{2m} \right] \delta(c_i, c_j), \quad (\text{Equation 11})$$

Where  $m$  is the total number of binding edges,  $A$  is the adjacency matrix (bottom in Figures 6G and 6H),  $k_i$  is the number of CaMKII bound to the  $i$ th CaMKII,  $c_i$  denotes the community of the  $i$ th CaMKII, and  $\delta(i, j)$  is the Kronecker delta.  $Q$  can be written as:

$$Q = \sum_{ci} \left[ \frac{L_{ci}}{m} - \left( \frac{k_{ci}}{2m} \right)^2 \right] \quad (\text{Equation 12})$$

Where  $ci$  denotes the community index, and  $L_{ci}$  is the number of intra-community links for community  $ci$ ,  $k_{ci}$  is the sum of the number of binding partners from all the CaMKII in community  $ci$ . In Equation 12, the first term represents the number of intra-community connections, and the second term represents the total number of connections. Thus,  $Q$  represents the relative contribution of intra-community connections.  $Q$  has a value in the range of  $[-1/2, 1]$ , and its higher value indicates a more modular network.